

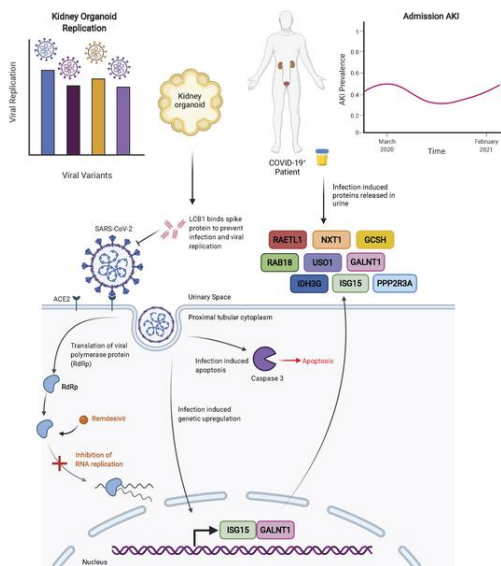
## Cross-validation of SARS-CoV-2 responses in kidney organoids and clinical populations

Louisa Helms, ... , Michael Gale, Jr., Benjamin S. Freedman

JCI Insight. 2021. <https://doi.org/10.1172/jci.insight.154882>.

Research In-Press Preview COVID-19 Nephrology

### Graphical abstract



Find the latest version:

<https://jci.me/154882/pdf>



# Cross-validation of SARS-CoV-2 Responses in Kidney Organoids and Clinical Populations

## AUTHORS

Louisa Helms<sup>1,2,3,4</sup>, Silvia Marchiano<sup>1,4,5,6,7</sup>, Ian B. Stanaway<sup>1,2,3</sup>, Tien-Ying Hsiang<sup>8</sup>, Benjamin Juliar<sup>1,2,3,4</sup>, Shally Saini<sup>4,9</sup>, Yan Ting Zhao<sup>4,9,10</sup>, Akshita Khanna<sup>4,5,7</sup>, Rajasree Menon<sup>11</sup>, Fadhl Alakwaa<sup>11</sup>, Carmen Mikacenic<sup>12,13</sup>, Eric D. Morrell<sup>1,13</sup>, Mark M. Wurfel<sup>1,13</sup>, Matthias Kretzler<sup>11,14</sup>, Jennifer L. Harder<sup>11</sup>, Charles E. Murry<sup>1,4,5,6,7,15</sup>, Jonathan Himmelfarb<sup>1,2,3</sup>, Hannele Ruohola-Baker<sup>4,9,10,16</sup>, Pavan K. Bhatraju<sup>1,3,13</sup>, Michael Gale Jr.<sup>8</sup>, Benjamin S. Freedman<sup>1,2,3,4,16†</sup>

## AFFILIATIONS

<sup>1</sup>Department of Medicine, University of Washington School of Medicine, Seattle WA 98109

<sup>2</sup>Division of Nephrology, University of Washington School of Medicine, Seattle WA 98109

<sup>3</sup>Kidney Research Institute, University of Washington School of Medicine, Seattle WA 98109

<sup>4</sup>Institute for Stem Cell and Regenerative Medicine, University of Washington School of Medicine, Seattle WA 98109

<sup>5</sup>Department of Laboratory Medicine and Pathology, University of Washington School of Medicine, Seattle WA 98109

<sup>6</sup>Division of Cardiology, University of Washington School of Medicine, Seattle WA 98109

<sup>7</sup>Center for Cardiovascular Biology, University of Washington School of Medicine, Seattle WA 98109

<sup>8</sup>Center for Innate Immunity and Immune Disease, Department of Immunology, University of Washington School of Medicine, Seattle WA, 98109

27 <sup>9</sup>Department of Biochemistry, University of Washington School of Medicine, Seattle WA, 98195

28 <sup>10</sup>Oral Health Sciences, School of Dentistry, University of Washington School of Medicine,  
29 Seattle WA, 98195

30 <sup>11</sup>University of Michigan, Department of Internal Medicine, Division of Nephrology

31 <sup>12</sup>Translational Research, Benaroya Research Institute, Seattle, WA, 98101

32 <sup>13</sup>Division of Pulmonary, Critical Care and Sleep Medicine, University of Washington School of  
33 Medicine, Seattle WA 98195

34 <sup>14</sup>University of Michigan, Department of Computational Medicine and Bioinformatics

35 <sup>15</sup>Sana Biotechnology, Seattle WA, 98102

36 <sup>16</sup>Department of Bioengineering, University of Washington, Seattle WA, 98105

37

38 † Correspondence:

39 Benjamin S. Freedman, Ph.D.  
40 Associate Professor  
41 University of Washington School of Medicine  
42 850 Republican St, Box 358056  
43 Seattle, WA 98109, USA  
44 Phone: +1 (206) 685-4653 E-mail: [benof@uw.edu](mailto:benof@uw.edu)  
45

46

47

48

49 **ABSTRACT**

50

51 Kidneys are critical target organs of COVID-19, but susceptibility and responses to infection  
52 remain poorly understood. Here, we combine SARS-CoV-2 variants with genome edited kidney  
53 organoids and clinical data to investigate tropism, mechanism, and therapeutics. SARS-CoV-2  
54 specifically infects organoid proximal tubules amongst diverse cell types. Infections produce  
55 replicating virus, apoptosis, and disrupted cell morphology, features of which are revealed in  
56 the context of polycystic kidney disease. Cross-validation of gene expression patterns in  
57 organoids reflect proteomic signatures of COVID-19 in the urine of critically ill patients indicating  
58 interferon pathway upregulation. SARS-CoV-2 viral variants Alpha, Beta, Gamma, Kappa, and  
59 Delta exhibit comparable levels of replication in organoids. Infection is ameliorated in *ACE2*<sup>-/-</sup>  
60 organoids and blocked via treatment with *de novo* designed spike binder peptides. Collectively,  
61 these studies clarify the impact of kidney infection in COVID-19 as reflected in organoids and  
62 clinical populations, enabling assessment of viral fitness and emerging therapies.

63 **INTRODUCTION**

64

65 Severe acute respiratory syndrome coronavirus 2 (SARS-CoV-2), first detected at the end of  
66 2019 in the Hubei province of China, has spread worldwide causing the coronavirus disease,  
67 COVID-19 (1). Despite substantial progress and therapeutic innovation, COVID-19 continues  
68 to spread and impact the globe. SARS-CoV-2 belongs to the viral family *Coronaviridae* in which  
69 three new coronaviruses have emerged from animal reservoirs in the past two decades causing  
70 serious illness and death: SARS-CoV, Middle East respiratory syndrome coronavirus (MERS-  
71 CoV), and now SARS-CoV-2 (2). In addition to respiratory distress, patients with COVID-19  
72 exhibit systemic symptoms that involve the kidneys, similarly to previous SARS-CoV and  
73 MERS-CoV outbreaks (3–5). Chronic kidney disease and its causes such as hypertension and  
74 diabetes are noted risk factors for developing severe COVID-19 disease, and COVID-19  
75 patients frequently develop acute kidney injury (AKI) (3, 6). Angiotensin-converting enzyme 2  
76 (ACE2) is the primary entry receptor for SARS-CoV-2 in many experimental models and is  
77 strongly expressed in the proximal tubular epithelial cells of the kidney, implicating the kidney  
78 as a target for SARS-CoV-2 infection (7–11). Multiple autopsy reports have suggested SARS-  
79 CoV-2 infection of the kidney, and several groups have isolated SARS-CoV-2 from infected  
80 patient urine, however, it remains unclear whether direct infection of the kidney is responsible  
81 for AKI and severity of COVID-19 disease, versus systemic effects resulting from pulmonary  
82 distress (12–17).

83

84 Human cellular and organoid model systems have played a valuable role in our understanding  
85 of SARS-CoV-2 infection mechanisms, interactions with key target organs, and the efficacy of  
86 COVID-19 therapeutics as they provide more complex physiological compositions and  
87 behaviors than standard 2D culture (18–24). Human models are particularly valuable because  
88 mice are not generally susceptible to SARS-CoV-2 without adaptation to mouse ACE2 (25).

89 Kidney organoids are segmented structures that resemble primitive nephrons, which can be  
90 differentiated *in vitro* from human pluripotent stem cells, including induced pluripotent stem (iPS)  
91 cells and embryonic stem (ES) cells (26–29). These organoid cultures contain diverse cell types  
92 in patterned, well-differentiated structural arrangements, an advantage over traditional primary  
93 cultures which consist primarily of dedifferentiated proximal tubular cells. Because human  
94 pluripotent stem cells are immortal, they are readily amenable to genome editing to produce  
95 isogenic pairs of mutant and control cell lines, enabling reconstitution of hereditary disease  
96 phenotypes such as polycystic kidney disease cystogenesis in derived organoids (28). Such  
97 cell lines cannot be readily established from primary cultures which typically senesce rapidly  
98 and have a much more limited proliferative potential (24). SARS-CoV-2 can infect kidney  
99 organoid cultures, a property that has been leveraged to test candidate therapeutics (19, 22).  
100 Because organoids contain multiple cell types, additional experiments are needed to determine  
101 which of these cell types are specifically infected by using novel fluorescence-reporter SARS-  
102 CoV-2 variants (30–33). The ability to co-localize SARS-CoV-2 infection with markers of  
103 apoptosis would provide critical insight into whether infection can produce direct cytotoxic  
104 effects simulating AKI, which were not detected in a recent study of somatic-derived kidney  
105 spheroids (34). It is also important to further apply this system to compare to clinical cohorts,  
106 viral variants of concern, and screen candidate therapeutics for safety and efficacy related to  
107 kidney disease.

108

109 Application of genome edited organoids to SARS-CoV-2 presents valuable opportunities to  
110 determine mechanisms of viral infection and assess the impact of pre-existing disease states  
111 (18, 28, 35–37). In this study, we cross-validate SARS-CoV-2's impact on kidney organoids  
112 and clinical data to investigate tropism, mechanism, and therapeutics. These findings provide  
113 clear evidence of SARS-CoV-2's kidney tropism, acute cytopathic effects, systemic and kidney-  
114 specific proteomic responses, and efficacy of COVID-19 therapeutics.

115

## 116 **RESULTS**

117

### 118 **SARS-CoV-2 infects organoid proximal tubules with pathogenic effects**

119

120 To assess the susceptibility of kidney organoid cell types to SARS-CoV-2 infection, we utilized  
121 an adherent differentiation protocol that produces nephron-like epithelial structures surrounded  
122 by a monolayer of stromal and endothelial cell types (28, 32). We exposed these human kidney  
123 organoid cultures to a multiplicity of infection (MOI) 10 of SARS-CoV-2/WA1 (SARS-CoV-2) and  
124 measured infection 72 hours later (Figure 1A). Using SARS-CoV-2 genetically engineered to  
125 express mNeonGreen (SARS-CoV-2-mNG), we observed that the fluorescent signal localized  
126 in epithelial kidney organoid structures, whereas the surrounding monolayer of stromal and  
127 endothelial cells was not infected (Figures 1B) (30). Viral RNA of SARS-CoV-2 was readily  
128 detected in infected cultures, indicating that virus had entered cells (Figure 1C). 72 hours post-  
129 infection, supernatants from organoids exposed to SARS-CoV-2 or SARS-CoV-2-mNG  
130 efficiently infected Vero cells and produced viral plaques, demonstrating functional virion  
131 production in kidney organoids (Figure 1D and Figure S1A). Immunofluorescence analysis of  
132 nephron markers in organoids exposed to SARS-CoV-2-mNG revealed specific infection of  
133 *Lotus tetragonolobus* lectin positive (LTL<sup>+</sup>) proximal tubules (Figure 1E). The strong binding of  
134 LTL to infected cells suggested that these were likely to be proximal rather than distal tubules  
135 (33). Podocytes were not generally infected, but individual podocytes (PODXL<sup>+</sup>) infected with  
136 SARS-CoV-2-mNG were occasionally observed by confocal microscopy (Figure S1B). Similarly,  
137 cells resembling the parietal epithelial cells of Bowman's capsule (CLDN1<sup>+</sup>) were not generally  
138 infected (Figure S1C) (33, 35). Using semi-automated image analysis quantification, we found  
139 that 12.4% of the total organoid area and 24.5% of the total LTL<sup>+</sup> area was infected, respectively,  
140 whereas infection of podocytes (PODXL<sup>+</sup>) was not significant (Figures 1F and S2A-D).

141

142 We found that the use of SARS-CoV-2-mNG was vital for establishing the tropism of infection  
143 in kidney organoids. In contrast to SARS-CoV-2-mNG, a commercially available GFP-  
144 expressing lentivirus pseudotyped for SARS-CoV-2 failed to productively infect kidney  
145 organoids or Vero cells (Figure S3A). This likely reflects inferior levels of infection by SARS-  
146 pseudotyped lentiviruses, compared to native virus (38). In addition, a commercially available  
147 antibody raised against SARS-CoV-2 nucleocapsid did not produce specific staining in  
148 organoids infected with SARS-CoV-2, but rather showed high background staining levels in  
149 stromal cells, necessitating our use of SARS-CoV-2-mNG to evaluate viral tropism (Figure  
150 S3B).

151

152 Close inspection of infected versus non-infected proximal tubules revealed swollen, rounded  
153 cells with a disruption of the smooth LTL patterning at the apical plasma membrane showing  
154 increased compartmentalization into bright foci (Figure 1G). Immunofluorescence analysis of  
155 cleaved caspase-3 was inconclusive because it was difficult to discern in these densely packed,  
156 three-dimensional structures (Figure S3C). Lactate dehydrogenase (LDH) release was not  
157 detectably increased in infected organoid supernatants, consistent with the observation that  
158 SARS-CoV-2 treatment was not overtly toxic to these cultures as a whole (Figure S3D). These  
159 findings reveal specific proximal tubular tropism of SARS-CoV-2 capable of producing  
160 replicating virus and disrupting tubular morphology.

161

### 162 **SARS-CoV-2 infects PKD cystic epithelium causing cytotoxicity**

163

164 Polycystic kidney disease (PKD) is the most common genetic cause of chronic kidney disease  
165 and a possible risk factor for developing severe COVID-19, but these patients are rare which  
166 has impeded large cohort studies (39). In polycystic kidney disease, expansive cysts form from

167 tubular epithelial cells, but whether PKD cysts are susceptible to SARS-CoV-2 infection is  
168 unknown. We assessed this with *PKD2*<sup>-/-</sup> organoids in suspension culture, which form cysts from  
169 proximal and distal tubules (37) (Figure 2A). Cystic organoids were infected with SARS-CoV-2  
170 and SARS-CoV-2-mNG and assessed for viral infection and replication via plaque assay and  
171 immunofluorescence staining (Figures 2B and S4A). A subpopulation of cyst-lining epithelial  
172 cells with LTL binding affinity (suggesting a proximal tubular origin) was infected selectively by  
173 SARS-CoV-2-mNG and caused cell swelling (Figures 2B and S4B). The percentage of infected  
174 area per cystic organoid was comparable to that of non-cystic organoids (Figure 2C).

175

176 Infection-induced apoptosis of cystic PKD epithelium was observed in infected organoids as  
177 indicated by significantly increased expression of cleaved caspase-3 and pyknotic nuclei in  
178 infected cells, compared to non-infected cells in the same organoid (Figure 2D-E). These  
179 indicators of cytotoxicity were more readily discerned in the thinner layer of cyst-lining epithelial  
180 cells than in denser organoid tubular structures without a PKD phenotype (see above, Figure  
181 S3C). Together, these data indicate that PKD cysts derived from proximal tubules are  
182 susceptible to SARS-CoV-2 infection in organoids, and that infection induces apoptosis in cystic  
183 epithelium.

184

### 185 **COVID-19<sup>+</sup> patient urine expresses signatures found in organoids**

186

187 To assess physiological relevance of the organoid model, we analyzed urinary proteins  
188 that characterize COVID-19 infection in prospectively enrolled critically ill patients with  
189 signs and symptoms suggestive of SARS-CoV-2 infection, who were placed under  
190 respiratory isolation by the treating physician (40) (Figure 3A). Positivity for COVID-19 was  
191 subsequently confirmed by RT-PCR (COVID-19<sup>+</sup>), while patients who tested negative  
192 provided a symptom-matched, critically ill control group (COVID-19<sup>-</sup>). In patients with an

193 indwelling catheter, we collected urine within 24 hours of intensive care unit admission  
194 from 61 COVID-19<sup>+</sup> and 59 COVID-19<sup>-</sup> patients. COVID-19<sup>+</sup> and COVID-19<sup>-</sup> patients were  
195 of similar mean age ( $56 \pm 17$  years and  $54 \pm 16$  years, respectively), while COVID-19<sup>+</sup>  
196 patients were more likely to be male (75% vs. 54%) and of Hispanic ethnicity (38% vs 7%)  
197 (Table 1). Despite COVID-19<sup>-</sup> patients having higher rates of chronic kidney disease,  
198 coronary artery disease and congestive heart failure, rates of AKI at the time of study  
199 enrollment were similar (58% in COVID-19<sup>+</sup> and 59% in COVID-19<sup>-</sup>). However, by the time  
200 of hospital discharge, receipt of acute renal replacement therapy was two-fold higher in  
201 COVID-19<sup>+</sup> compared to COVID-19<sup>-</sup> patients (15% vs 7%).

202

203 Urinary proteomes indicated a negative relationship between protein size and relative  
204 abundance (Spearman's rank correlation,  $\rho = -0.05$ ), whereas patient plasma exhibited  
205 no significant relationship of this kind, likely reflecting the size selectivity of the glomerular  
206 filtration barrier (Figure 3B and Figure S5A). Proteins too large to be efficiently filtered  
207 were nevertheless detected in these urines, including cubilin (CUBN) and megalin (LRP2),  
208 receptors that are strongly expressed in the brush border of kidney proximal tubular cells.  
209 Thus, urinary proteomes contained both filtered proteins originating from the plasma, as  
210 well as non-filtered proteins originating from the kidneys and urinary tract.

211

212 We compared 4,984 urinary proteins between these patients with and without COVID-19.  
213 Using this urine proteomic data, we performed a Gene Ontology pathway analysis which  
214 identified 207 pathways as significantly differentially abundant with a false discovery rate  
215 (FDR)  $< 0.05$ . Two pathways, interleukin-10 (IL-10) production ( $p = 3.83 \times 10^{-6}$ , FDR =  
216 0.006) and interferon-stimulated gene 15 (ISG15) protein conjugation ( $p = 4.79 \times 10^{-6}$ ,  
217 FDR = 0.006), met the Bonferroni correction threshold of  $p < 7.80 \times 10^{-6}$ . The third most  
218 significant pathway was interferon gamma production ( $p = 8.00 \times 10^{-6}$ , FDR = 0.006)

219 (Figure 3C).

220

221 Nine individual proteins were significantly higher in COVID-19<sup>+</sup> patients adjusting for age,  
222 gender and body mass index with an FDR < 0.1 (Figure 3D): ISG15, polypeptide N-  
223 acetylgalactosaminyltransferase 1 (GALNT1), isocitrate dehydrogenase (NAD(+)) 3 non-  
224 catalytic subunit gamma (IDH3G), glycine cleavage system protein H (GCSH), Ras-  
225 related protein 18 (RAB18), nuclear transport factor 2 like export factor 1 (NXT1), protein  
226 phosphatase 2 regulatory subunit B"Alpha (PPP2R3A), USO1 vesicle transport factor  
227 (USO1), and retinoic acid early transcript 1L (RAET1L) (Figure 3E). No individual proteins  
228 were found to be downregulated in COVID patient urine at this FDR cutoff. A refined linear  
229 regression analysis of the proteomic hits (FDR < 0.05) further identified 23 upregulated  
230 proteins, of which the top nine are the same as described above and revealed 2 down-  
231 regulated proteins in COVID-19<sup>+</sup> patient urine, hypoxanthine phosphoribosyltransferase 1  
232 (HPRT1) and CD5 molecule-like (CD5L) (Figure S6A).

233

234 Transcripts of eight of these nine proteins were increased in kidney organoids infected  
235 with SARS-CoV-2 compared to their MOCK infected controls, including ISG15 and  
236 GALNT1 which were significantly upregulated (Figure 3F). We assessed the cellular  
237 origins of the nine upregulated proteomic hits in a COVID-19<sup>+</sup> urine single-cell RNA seq  
238 database, which revealed expression levels of all the hits in urothelial and proximal tubular  
239 cells, and a variety expressed in immune and myeloid cells (Figure S6B-C) (41).  
240 Collectively, these expression signatures suggested that SARS-CoV-2 infection can  
241 induce an interferon response in kidney epithelial cell types similar in both patients and  
242 organoids (42–45).

243

244 **SARS-CoV-2 variants show similar rates of infection in kidney organoids**

245

246 SARS-CoV-2 is a positive-sense, single-stranded RNA virus that utilizes an RNA dependent  
247 RNA polymerase carrying a high mutation rate, up to one million times higher than its hosts'  
248 DNA polymerase(46). Higher mutation rates correlate with enhanced virulence of emerging viral  
249 strains and are suggested to produce SARS-CoV-2 viral variants with enhanced infectivity, such  
250 as the Delta variant (47–49). Formal studies directly comparing infection rates between variants  
251 of SARS-CoV-2 are required to draw this conclusion. Moreover, it is unknown if SARS-CoV-2  
252 variants might exhibit differential tropism for the respiratory tract, which is the primary route of  
253 infection, versus extra-pulmonary organs, such as the kidney.

254

255 To assess whether SARS-CoV-2 variants exhibit altered viral fitness in kidney organoids, we  
256 infected kidney organoids with five viral variants: USA-WA1 (WA1), B.1.351-HV001 (Beta),  
257 B.1.1.7 (Alpha), P.1 (Gamma), B.1.617.1 (Kappa), and B.1.617.2 (Delta) (Table 2). Notably, the  
258 Delta variant we used for infections has a deletion in ORF7a that may influence virulence,  
259 although this strain is nevertheless associated with Delta outbreaks in human populations (50,  
260 51). qRT-PCR analysis of RNA extracted from infected organoids demonstrated variable levels  
261 of detectable SARS-CoV-2 transcript, which were not statistically significant between variants  
262 (Figure 4A). Interestingly, supernatants from infected kidney organoids reveal significantly  
263 decreased levels of replicating virus from the Alpha, Gamma, Kappa, and Delta variants,  
264 compared to one of the originally isolated WA1 strains (Figure 4B-C). Additionally, LDH release  
265 from infected kidney organoids was not significantly different between viral strains, nor  
266 heightened compared to mock infected controls (Figure S7A).

267

268 To assess whether rates of admission AKI, dialysis, or death change over time in our patient  
269 cohort, we plotted the prevalence at each patient's admission, of admission AKI, inpatient  
270 dialysis and in-hospital death over time using that patient and the next nine COVID-19<sup>+</sup> patients

271 admitted to the ICU (Figure 4D). Death, dialysis, and AKI all had relatively low variance over  
272 time: AKI hovering around 40% prevalence, dialysis around 20%, and death around 50%  
273 between March, 2020 to February, 2021. While comprehensive variant sequencing data was  
274 unavailable in our COVID-19<sup>+</sup> patient cohort, in Washington State, the WA1 variant was the  
275 predominant viral strain in March 2020, and the Alpha, Beta, and Gamma variants were  
276 detected in the US in January, 2021 and Kappa and Delta detected March-May of 2021, while  
277 rates of AKI and dialysis remained steady in our patient cohort (52–55).

278

### 279 **ACE2 is an essential viral entry pathway for SARS-CoV-2 infection**

280

281 Susceptibility of kidney organoids to SARS-CoV-2 infection is thought to depend upon  
282 expression of ACE2, but genetic proof of this is lacking. To assess this, we utilized genetically  
283 modified *ACE2*<sup>-/-</sup> stem cell lines, compared to *ACE2*<sup>+/+</sup> controls (Figure 5A) (18). *ACE2*<sup>-/-</sup> kidney  
284 organoids differentiated normally (Figure S8A). When exposed to SARS-CoV-2-mNG, however,  
285 *ACE2*<sup>-/-</sup> organoids did not express detectable mNG-fluorescence, in contrast to *ACE2*<sup>+/+</sup> controls  
286 (Figure 5B-C). Supernatants from *ACE2*<sup>-/-</sup> organoid cultures showed 85% fewer viral particles  
287 than supernatants from *ACE2*<sup>+/+</sup> controls and were not significantly different in viral production  
288 from MOCK infected controls (Figure 5D).

289

290 A commercially available antibody raised against ACE2 (Antibody 1, aa18-740) exhibited high  
291 levels of background in healthy or infected kidney organoids due to the density of these cultures  
292 but achieved lower background and higher specificity in cystic PKD organoids which possess a  
293 single-cell epithelium (Figure S8B-C). Antibody 1 appeared more specific in organoids than  
294 another commercially available antibody (Antibody 2, aa190-230) (Figure S8D). The relatively  
295 poor performance of these antibodies in kidney organoids was not due to general non-  
296 specificity, as Antibody 1 localized specifically to proximal tubular cells in cryosections of human

297 developing kidney tissue, and Antibody 2 localized to the proximal tubules of an adult mouse  
298 (Figure S9A-B). Therefore, we hypothesized that ACE2 was expressed in organoids but could  
299 not be readily detected due to the absence of well-differentiated brush border in these  
300 structures, which we have diagnosed previously (28, 33, 56).

301

302 Indeed, transcripts encoding both ACE2 and the transmembrane serine protease 2  
303 (TMPRSS2), a co-receptor involved in priming coronavirus for cell entry, were expressed in  
304 organoid cultures (41). Interestingly, ACE2 expression trended downward in response to SARS-  
305 CoV-2 infection, although not statistically significant (Figure S9C). We previously performed an  
306 unbiased single cell RNA sequencing (scRNA-seq) analysis of these kidney organoid cultures,  
307 which indicated a total of 11 distinct cell clusters(32). Amongst the 6 of these clusters believed  
308 to represent kidney cell types, ACE2 was detected specifically in proximal tubules or early  
309 proximal tubules, albeit at relatively low expression levels. These same clusters also expressed  
310 several other proposed SARS-CoV-2 entry factors, including *TMPRSS2*, *FURIN*, *BSG* (basigin),  
311 *ENPEP* (glutamyl aminopeptidase), *ANPEP* (alanyl aminopeptidase), *CTSL* (cathepsin L), and  
312 *DPP4* (dipeptidyl-peptidase 4), the latter being particularly abundant in proximal tubules. Many  
313 of these other entry factors were expressed in additional cell clusters, such as podocytes or  
314 stromal cells, often at greater abundance than in proximal tubules (Figure S9D). Overall, these  
315 results indicated that SARS-CoV-2 infection of kidney organoids is predominantly mediated by  
316 ACE2, and that ACE2 expression may be affected by SARS-CoV-2 infection (57).

317

### 318 **Therapeutics reduce SARS-CoV-2 infection and replication in kidney organoids**

319

320 The emergence of SARS-CoV-2 has sparked the rapid development of novel therapeutics  
321 aimed to block viral infection and replication (58). The nucleotide analogue prodrug remdesivir  
322 was granted emergency use authorization (EUA) for the treatment of COVID-19 in May 2020

323 for its ability to inhibit viral RNA-dependent RNA polymerase (59). While studies have shown  
324 that remdesivir treatment in AKI and CKD patients is tolerated well, the active metabolite of  
325 remdesivir is eliminated by the kidneys and has been reported to increase chances of  
326 developing AKI in remdesivir-treated patients (60–62). To investigate the efficacy of remdesivir,  
327 we infected kidney organoids with SARS-CoV-2 (WA1) or SARS-CoV-2-mNG, and then treated  
328 the infected organoids with a 2  $\mu$ M dose of remdesivir immediately after infection (Figure 6A).  
329 This dose was previously determined to be non-toxic to control organoids in titrations of the  
330 compound, whereas doses > 8  $\mu$ M exhibited noticeable toxicity (Figure S10A). Comparable  
331 levels of toxicity via Calcein AM/Propidium Iodide staining were noted between control and  
332 cystic *PKD2*<sup>-/-</sup> organoids after 72 hours of treatment (Figure S10B). Supernatants from treated  
333 and untreated organoids were collected, revealing 71.4%  $\pm$  18% reduced replicated virus in the  
334 remdesivir treated organoids (Figures 6B and S10C). Immunofluorescence analysis of  
335 remdesivir-treated and untreated organoids indicated comparable levels of SARS-CoV-2-mNG  
336 infection and intact podocytes and proximal tubules, suggesting that remdesivir treatment did  
337 not have an overtly nephrotoxic effect after 72 hours of treatment (Figure S10D). These data  
338 suggest that remdesivir significantly reduces viral replication of infected kidney organoids and  
339 supports short-term safety of remdesivir treatment in kidney cells at the efficacious dose, while  
340 cautioning that overdose of the drug may be counterproductive for the kidneys.

341

342 While remdesivir appears to show efficacy *in vitro*, it is not efficacious *in vivo* in lowering  
343 mortality or reducing infection in COVID-19 patients, necessitating the development of  
344 alternatives (63, 64). The *de novo* designed protein, LCB1, was specifically designed to bind  
345 the receptor binding domain of SARS-CoV-2's spike protein at picomolar concentrations and  
346 has been estimated to have six-fold greater potency than monoclonal antibodies but has not yet  
347 tested efficacy in renal tissues (Figure 6C) (65, 66). To assess whether LCB1 can block SARS-  
348 CoV-2 infection and replication in a kidney-relevant system we preincubated 0  $\mu$ M-30  $\mu$ M of

349 LCB1 with an MOI of 10 of SARS-CoV-2 for 1 hour, and then added the LCB1:virus mixture to  
350 kidney organoids (Figure 6D). qRT-PCR analysis of RNA extracted from infected organoids  
351 demonstrated an LCB1 dose-dependent decrease of detectable SARS-CoV-2 transcript, with  
352 significantly different levels at 0.03  $\mu$ M and higher (Figure 6E). Supernatants collected from  
353 infected organoids were assessed via plaque assay, revealing a dose-dependent decrease in  
354 viral particles, starting at  $\geq 0.03 \mu$ M, with complete abrogation at the 3  $\mu$ M and higher doses  
355 (Figure 6F). Thus, LCB1 can efficiently block SARS-CoV-2 infection at levels sufficient to  
356 prevent viral replication in human kidney organoids.

357

## 358 **DISCUSSION**

359

360 Renal involvement in SARS-CoV-2 infection and COVID-19 severity is widely acknowledged,  
361 but challenges remain in assessing direct and indirect effects of SARS-CoV-2 infection on the  
362 kidneys. Utilizing a fluorescent SARS-CoV-2 reporter virus with infectious properties  
363 comparable to native SARS-CoV-2, we directly demonstrate that the proximal tubules are  
364 uniquely infected in these cultures (30). Our experiments utilizing *ACE2*<sup>-/-</sup> kidney organoids  
365 rigorously demonstrate the requirement for ACE2 mediated viral entry in kidney organoids,  
366 despite lacking a well-differentiated brush border. A limitation of the current system is that  
367 organoids may reflect a more fetal or dedifferentiated state, compared to adult kidneys in vivo,  
368 and lack collecting ducts (28, 31, 33, 67). This must be considered when extrapolating findings  
369 from organoids to the clinical context.

370

371 Similarly, PKD cysts, which feature a more squamous epithelium, contain cells expressing  
372 ACE2 and LTL that are susceptible to SARS-CoV-2 infection, which likely derive from proximal  
373 tubules (37). The extent of infection observed in cystic organoids is similar to control (non-cystic)  
374 organoids, suggesting that PKD neither enhances nor protects against SARS-CoV-2, consistent

375 with a clinical report in which ADPKD patients did not have significantly increased major COVID-  
376 19 outcomes (68). Evidence of cytotoxicity was more readily discerned in PKD cysts than in  
377 non-cystic tubules, although this may be attributable to improved optics in the cysts.  
378 Alternatively, it is possible that increased cell division in the cysts may contribute to a greater  
379 susceptibility to injury, as is observed in purified human kidney cells during proliferative  
380 expansion in monolayer cultures (34). PKD patients are rare, and none were found amongst  
381 our clinical cohort. Further studies are warranted regarding the potential of SARS-CoV-2 to  
382 infect and injure PKD cysts in patients compared to non-cystic kidney tissue.

383

384 An important question is whether SARS-CoV-2 infection can lead to cytotoxicity in kidney  
385 epithelial cells, similar to pulmonary epithelium (69–71). Confocal analysis of infected organoid  
386 proximal tubules reveals cell swelling and disrupted LTL marker expression. Cleaved caspase-  
387 3 expression and pyknotic nuclei in infected PKD organoids further substantiates infection-  
388 induced cytotoxicity. Swelling of the cells might also be suggestive of hypertrophy, which is  
389 observed in kidney proximal tubular cells after AKI (72). The higher rates of cell division in our  
390 organoid cultures, particularly those with PKD, may contribute to the enhanced sensitivity of  
391 these cells to infection-induced injury, compared to spheroids derived from human fetal kidney  
392 tissue, which do not show an AKI phenotype (34). Thus, these phenotypes likely reflect an  
393 innate, AKI-like program triggered by infection in these human proximal tubular cells.

394

395 Our prospective cohort of COVID-19<sup>+</sup> and COVID-19<sup>-</sup> patients revealed proteomic upregulation  
396 of nine proteins in COVID-19<sup>+</sup> patient urine, a signature that was also reflected in kidney  
397 organoids and kidney cells in patient urines (41). Upregulation of these genes produces  
398 significant differences in IFN and IL-10 gene ontology pathways. This supports the hypothesis  
399 that AKI in COVID-19 patients may arise as a direct result of kidney infection or a combination  
400 of both systemic and kidney specific response to infection. *In vivo*, such a scenario would

401 necessitate levels of viremia sufficient to spread infection to kidney cells expressing ACE2.  
402 Rates of viremia are quite variable, but recent work suggests that viremia may be higher in  
403 critically ill COVID-19 patients (73–75). Once infected, such cells might undergo apoptosis to  
404 clear the infection from the kidneys, which would make it difficult to detect after the fact. One  
405 limitation of urinary proteomics is that low molecular weight proteins can be filtered into the urine  
406 from the blood, thus detection of a kidney-specific gene expression signature is challenging and  
407 requires cross-validation in organoids and other models.

408

409 Interestingly, COVID-19 patients with risk allele genotypes for apolipoprotein L1 (APOL1) have  
410 been shown to exhibit a collapsing glomerulopathy phenotype (76, 77). Podocytes were rarely  
411 infected in our organoids, likely due to the relatively low levels of ACE2 in these cells (33, 78).  
412 In previous work, we have shown that organoids at baseline do not express APOL1, but  
413 expression can be induced by treating the cultures with interferon gamma (79). In this regard, it  
414 is interesting that a prominent signature of COVID-19 in our AKI patient cohort relates to  
415 interferon gamma signaling, which is a known inducer of APOL1 (79–82). Thus, our study  
416 suggests that the collapsing glomerulopathy phenotype in COVID-19<sup>+</sup> risk allele patients may  
417 be a consequence of APOL1 induction in podocytes following interferon gamma exposure,  
418 rather than direct infection by the virus. Additional studies are needed to determine the precise  
419 impact of APOL1 mutations in SARS-CoV-2 induced collapsing glomerulopathy and the role of  
420 interferon gamma in this process.

421

422 Remdesivir (Veklury) was granted emergency use authorization by the U.S. Food and Drug  
423 Administration in May of 2020 for treatment of COVID-19, but more recently, the efficacy of  
424 remdesivir for COVID-19 has been challenged (63, 64). The safety and efficacy of remdesivir  
425 has not been fully assessed in patients with kidney disease. In animal studies, the kidney was  
426 identified as the primary target organ of remdesivir toxicity, and higher levels of remdesivir's

427 metabolite GS-441524 were found in patients with renal dysfunction, suggesting an added risk  
428 with remdesivir treatment in those with CKD (83, 84). At a dose of 2  $\mu\text{M}$ , remdesivir was able to  
429 significantly reduce viral replication in infected kidney organoids without acutely damaging the  
430 epithelial cells, suggesting that a dose providing a balance of safety and efficacy may be  
431 achievable. Higher doses were, however, observed to show toxicity in both healthy and control  
432 organoids. The  $C_{\text{max}}$  after injection of a 150 mg dose of remdesivir is 2280 ng/mL, or 3.78  $\mu\text{M}$   
433 concentration in blood, very close to our effective, non-toxic dose used in kidney organoids (83).  
434 Our findings suggest that if remdesivir is administered, it should be used with caution to avoid  
435 over-dosing, particularly in patients with kidney disease. The novel protein, LCB1, designed to  
436 prevent SARS-CoV-2's receptor binding domain interaction with ACE2, presents a promising  
437 new strategy for treating COVID-19 (65). LCB1 doses of 0.03  $\mu\text{M}$  and higher were able to  
438 significantly reduce SARS-CoV-2 transcript levels in organoids infected with an MOI of 10, and  
439 the number of viral particles in kidney organoid supernatants. These data suggests that LCB1  
440 can efficiently bind to SARS-CoV-2 and prevent viral replication, even in organoids with  
441 detectable infections. LCB1 was designed specifically against the receptor binding domain of  
442 the SARS-CoV-2/WA1 variant isolated in 2020. As variants emerge, these spike binder proteins  
443 may lose their potency if critical binding domains are mutated, necessitating new designs (85).

444

445 Indeed, our data suggest that emerging viral variants may also have distinct capacity for  
446 infecting the kidney and may lose that capacity with evolving mutagenesis. While all the variants  
447 tested – Alpha, Beta, Gamma, Kappa, Delta – have reported heightened rates of transmission,  
448 controlled experiments are required to measure viral fitness in specific organ systems (86–88).  
449 Our data suggest that infection rates of these viral variants are statistically comparable, but  
450 replication rates in the Alpha, Gamma, Kappa, and Delta strains are significantly decreased,  
451 reflecting a potential loss of kidney-specific viral replication fitness in those strains. Notably, the  
452 Delta strain used in our experiments has a deletion in ORF7a which may contribute to its lack

453 of virulence due to its inability to antagonize the IFN pathway, although deletions in ORF7a  
454 have not been linked with significant functional consequences (30, 89, 90). The SARS-CoV-2-  
455 mNG variant we use has the mNG cassette inserted into ORF7A which demonstrates slightly  
456 decreased viral replication, but not significantly so (30). Nevertheless, deletions in Delta's  
457 ORF7a have been linked with outbreaks in Australia and Uruguay, suggesting this strain retains  
458 substantial viral fitness (50, 51). The overall organoid infection and replication findings are  
459 consistent with clinical observations of decreasing incidence rates of AKI during the pandemic  
460 (91). These data could suggest that viral variants may have differential virulence in extra-  
461 pulmonary organs and, in turn, explain differences in clinical rates of AKI and dialysis during the  
462 pandemic. It will be vital to collect both viral sequencing data and clinical data in large cohorts  
463 to conclude whether viral variants are linked with changes in rates of AKI.

464

465 Collectively, our results reveal that SARS-CoV-2 can directly infect and damage kidney tubular  
466 epithelial cells in organoids derived from pluripotent stem cells (92). In this regard, kidney  
467 organoid epithelium may model features of lung epithelium in acute respiratory distress  
468 syndrome relevant to COVID-19. Data from a controlled human cohort of COVID-19 patients  
469 support the physiological relevance of the findings in organoids. The remarkable tropism  
470 observed in these organoids, their ability to reveal physiologically relevant injury, and their  
471 accessibility to genome editing, together with the availability of urine samples from patients for  
472 proteomic analysis, combine to establish a powerful system for studying COVID-19 renal  
473 pathophysiology and developing therapeutics (19, 22, 85).

474

## 475 **METHODS**

476

477 **Cell Generation.** Experiments were performed using wild-type WTC11 iPS and H9 ES cell  
478 lines, and a single *PKD2*<sup>-/-</sup> and two *ACE2*<sup>-/-</sup> clones (WTC11 background), generated and

479 characterized as described previously (18, 28). Altogether these represent two distinct genetic  
480 backgrounds, genders, and cell types: (i) male WTC11 iPS cells (Coriell Institute Biobank,  
481 GM25256) and (ii) female H9 ES cells (WiCell, Madison Wisconsin, WA09).

482

483 **Kidney organoid differentiation.** Work with iPS and ES cells was conducted under the  
484 approval and auspices of the University of Washington Embryonic Stem Cell Research  
485 Oversight Committee. Specific cell lines used in this study are described below and are sourced  
486 from commercially available iPS and ES cell lines obtained with informed consent. Stem cell  
487 stocks were maintained in mTeSR1 media with daily media changes and passaging using  
488 Accutase (STEMCELL Technologies). 1,000-6,000 cells per well were placed in each 24-well  
489 plate pre-coated with 300  $\mu$ L of DMEM-F12 containing 0.2 mg/mL Matrigel and sandwiched the  
490 following day with 0.2 mg/mL Matrigel in mTeSR1 (STEMCELL Technologies) to produce  
491 scattered, isolated spheroid colonies. 48 hrs after sandwiching, spheroids were treated with  
492 12 $\mu$ M CHIR99021 (Tocris Bioscience) for 36h, then changed to RB (Advanced RPMI + 1X  
493 Glutamax + 1X B27 Supplement, all from Thermo Fisher Scientific) and replaced every 3 days  
494 thereafter. Organoids were differentiated for 21 days from the time of plating, at which time  
495 tubular structures had formed. Gene edited *PKD2*<sup>-/-</sup> organoids were picked from the adherent  
496 plate at day 21, placed in suspension culture with RB media replaced every 3 days until day 30  
497 when cyst growth was prominent (37).

498

499 **SARS-CoV-2 generation.** All experiments using live virus were performed in the Biosafety  
500 Level 3 (BSL-3) facility at the University of Washington in compliance with the BSL-3 laboratory  
501 safety protocols (CDC BMBL 5th ed.) and the recent CDC guidelines for handling SARS-CoV-  
502 2. Before removing samples from BSL-3 containment, samples were inactivated by Trizol or 4%  
503 paraformaldehyde, and the absence of viable SARS-CoV-2 was confirmed for each sample by  
504 plaque assays. SARS-Related Coronavirus 2, Isolate USA-WA1/2020 (SARS-CoV-2) and

505 icSARS-CoV-2mNG (SARS-CoV-2-mNG) were obtained from BEI Resources (NR-52281) and  
506 the University of Texas (30). Isolate 501Y.V2.HV001 (B.1.351) containing  
507 E484K/N501Y/D614G mutations along with furin cleavage site point mutation was obtained  
508 from Alex Sigal, AHRI (African Health Research Institute) and amplified in Vero-hACE2-  
509 TMPRSS2 cells upon reception. Virus stocks generated were tittered on VeroE6-TMPRSS2  
510 cells. SARS-CoV-2 isolates hCoV-19/England/204820464/2020 (NR-54000), hCoV-  
511 19/Japan/TY7-503/2021(NR-54982), hCoV-19/USA/CA-SU-15\_S02/2021 (NR-55486), and  
512 hCoV-19/USA/PHC658/2021 (NR-55611) were obtained through BEI Resources, NIAID, NIH  
513 and propagated in Vero cells (USAMRIID). Briefly, Vero cells were maintained in DMEM (Gibco)  
514 supplemented with 10% heat-inactivated FBS, 100 U/mL penicillin, and 100 U/mL streptomycin  
515 at 37 °C in a 5% CO<sub>2</sub> humidified incubator. To generate virus stock, cells were washed once  
516 with DPBS and infected with SARS-CoV-2 in serum-free DMEM. After 1 h of virus adsorption,  
517 the inoculum was replaced with DMEM supplemented with 2% heat-inactivated FBS, and cells  
518 were incubated at 37 °C in a 5% CO<sub>2</sub> incubator until ~70% of cells manifested cytopathic  
519 effects. The virus was harvested by collecting the culture supernatant followed by centrifugation  
520 at 3,000 g for 15 min at 4 °C to remove the cell debris. Virus titer was then measured by plaque  
521 assay on Vero cells (as described below), and stocks were stored at -80°C.

522

523 **SARS-CoV-2 titering.** Viral preparations and culture supernatant from SARS-CoV-2-infected  
524 kidney organoids were tittered using a plaque assay. Briefly, 350,000 Vero cells were seeded  
525 in 12-well plates and incubated for 1 h at 37 °C with 10-fold dilutions of virus-containing media.  
526 A 1:1 solution 1.8% cellulose suspension in water (Sigma) and 2X DMEM supplemented with  
527 4% heat-inactivated FBS, L- glutamine, 1X antibiotic-antimycotic (Gibco), and 220 mg/mL  
528 sodium pyruvate was layered on top of the cells, followed by incubation at 37 °C for 2 days.  
529 After fixing with 10% formaldehyde, the cellulose layer was removed and cells were stained with

530 0.5% crystal violet solution in 20% ethanol. Plaques were counted, and the virus titer in the  
531 original sample was assessed as plaque- formation unit per mL (PFU/mL).

532

533 **Fusion Forming Assay.** Viral culture supernatants from Delta variant supernatants were  
534 counted using a fusion forming assay rather than plaque assay due to their small size. The  
535 protocol is the same as the titrating protocol up to the cellulose layer removal step. After  
536 cellulose layer removal, fixed cells were washed with FFA wash buffer: 1X PBS with 0.05%  
537 Triton X-100 (Sigma). SARS-CoV-2 Nucleocapsid (Sino Biological 40143-R019-100, 1:8000)  
538 was added in FFA staining buffer: 1X PBS with 1 mg/ml Saponin (Sigma), and incubated  
539 overnight at 4 °C. The following day, cells were washed 3X with FFA wash buffer, and then  
540 incubated with goat anti-rabbit IgG HRP antibody (Bio-Rad 1706515, 1:5000) in FFA staining  
541 buffer for two-three hours at 4 °C. Cells were washed 3X with FFA wash buffer. TrueBlue  
542 Substrate (SeraCare) was added to cells, incubated for 10 minutes or until blue spots are visible  
543 with minimal background. Cells were then washed with water to quench the reaction and blue  
544 spots were counted and calculated based upon the volume of supernatant added as fusion  
545 forming units per mL (FFU/mL).

546

547 **Viral infection with and without therapeutic treatments.** SARS-CoV-2 was diluted to the  
548 desired MOI in serum-free DMEM and incubated on kidney organoids for 1 h at 37 °C (non-  
549 infected MOCK controls were incubated with DMEM only). Organoids were then washed with  
550 DPBS and cultured in RB media. Remdesivir (Selleck Chemicals) treatment involved adding 2  
551 µM remdesivir to RB media post 1 h viral incubation. LCB1 spike binder was mixed in a 1:1 ratio  
552 with diluted virus and incubated for 1 h at 37 °C prior to adding to organoids.

553

554 **Gene expression analysis and viral RNA detection.** Infected organoids were washed once  
555 with DPBS and incubated with 500 µl per well of Trizol reagent (Invitrogen) for 30 min at room

556 temperature. RNA was purified using the Direct-zol RNA Miniprep (Zymo Research). cDNA was  
557 synthesized using SuperScript IV Reverse Transcriptase per the manufacturer's instructions  
558 (ThermoFisher Scientific). Quantitative real-time reverse transcription (qRT-PCR) was  
559 performed with PowerUp SYBR Green Master Mix and the following forward and reverse  
560 primers: SARS-CoV-2-E, F: GAACCGACGACGACTACTAGC, R:  
561 ATTGCAGCAGTACGCACACA, ACE2, F: CCATCAGGATGTCCCGGAG, R:  
562 TGGAGGCATAAGGATTTTCTCCA, TMPRSS2, F: TCGAAGAACAATATCTGGTGGCT, R:  
563 GATTAGCCGTCTGCCCTCATTT, ISG15, F: GAGAGGCAGCGAACTCATCT, R:  
564 CTTCAGCTCTGACACCGACA, NXT1, F: GTTGTCATCTGTGGATCAGTGAA, R:  
565 CTACAGAGCTAGGGCTGAATGAA, USO1, F: GAAAGAACAGTTGCTCAGGGTTC, R:  
566 TGTTTGTATTTTGCTTCCCGTC, GALNT1, F: GGCTTGCATTTCTTTTCCTAAAT, R:  
567 TTGCCAACAGACTGCTCTACATA, PPP2R3A, F: CAGGAGGATTTTCATCCCTCTACT, R:  
568 TCGAAGTAATTTTCCACTCAA, IDH3G, F: CACAAGGCCAACATCATGAAACT, R:  
569 TCCACAATCATGTTCTCGAAGGT, RAB18, F: GAACTTGCAGCAACAATAGGTGT, R:  
570 AACACCCTGTGCACCTCTATAAT, GCSH, F: GGAAAGTGTGAAAGCTGCTAGTG, R:  
571 TCTTGATCAGCCAACCATCTTCA, beta-actin, F: GCGAGAAGATGACCCAGATCAT, R:  
572 GGATCTTCATGAGGTAGTCAGTC.

573

574 **Immunostaining.** Immunostaining followed by confocal microscopy was used to localize  
575 various proteins and transporters in the cysts and organoids. Prior to staining, organoids were  
576 fixed in 4% PFA for 30 mins at room temperature. After fixing, samples were washed in PBS,  
577 blocked in 5% donkey serum (Millipore)/0.3% Triton-X-100/PBS, incubated overnight in 1%  
578 bovine serum albumin/0.3% Triton-X-100/10 $\mu$ M CaCl<sub>2</sub>/PBS with primary antibodies, washed,  
579 incubated with Alexa-Fluor secondary antibodies (Invitrogen), washed and imaged. Primary  
580 antibodies or labels include Biotinylated LTL (Vector Labs B-1325, 1:500), E-Cadherin (Abcam  
581 ab11512, 1:500), hPODXL (R&D Systems AF1658, 1:500), ACE2 (Antibody 1: R&D Systems

582 AF933, 1:40, Antibody 2: Novus, #sn0754, 1:100), Cleaved caspase-3 (Cell Signaling  
583 Technology, 9661S, 1:100), Claudin-1 (Abcam 15098, 1:300),  
584 and SARS-CoV-2 Nucleocapsid (Sino Biological 40143-R019-100, 1:50). Live and dead  
585 staining used Calcein AM (Invitrogen) and Propidium Iodide (Thermo Fisher) per manufacturer's  
586 instructions. Fluorescence images were captured using a Nikon A1R inverted confocal  
587 microscope with objectives ranging from 10X to 60X. Note: we were unable to co-localize the  
588 infected with distal tubules (E-cadherin<sup>+</sup>), due to overlap in spectra between the secondary  
589 antibody and SARS-CoV-2-mNG.

590

591 **Immunohistochemistry.** Kidneys from a male 8-week-old C57BL/6J mouse were collected,  
592 paraffin embedded, sectioned, deparaffinized, quenched with 3 volumes of hydrogen peroxide  
593 in methanol, heat induced epitope retrieval in 1 mM EDTA, and blocked for 1 hour in 1.5%  
594 normal goat serum in PBS. Sections were then stained with ACE2 primary antibody (Novus,  
595 #sn0754, 1:100), washed, and stained with secondary antibody (Goat anti-rabbit biotin,  
596 ab64256) prior to imaging using an Olympus BX41 microscope at 40X.

597

598 **Patient Cohort and Clinical Data Collection.** The **COVID-19 Host Response and Clinical**  
599 **Outcomes (CHROME)** study began enrolling critically ill hospitalized patients suspected of  
600 SARS-CoV-2 infection in April 2020. This analysis included the first 120 patients enrolled in  
601 CHROME with an indwelling bladder catheter for collection of urine. Details of study enrollment  
602 have been previously published (40). In brief, subjects were eligible if they were admitted to an  
603 ICU for COVID-19 as defined by having symptoms suggestive of SARS-CoV-2 infection (fever,  
604 respiratory symptoms including cough/shortness of breath, or sore throat) and one of the  
605 following: 1) any respiratory support with supplemental oxygen or an oxygen saturation of <  
606 94% on ambient air; or 2) any chest radiographic abnormality. A case of COVID-19 was defined

607 by a positive reverse-transcriptase–polymerase-chain-reaction (RT-PCR) for SARS-CoV-2 from  
608 a nasopharyngeal swab. The University of Washington IRB approved all studies (STUDY9763).

609

610 **Sample collection, proteomic platform and quality control.** Urine was collected within 24  
611 hours of ICU admission. Peripheral blood was collected into EDTA anti-coagulant tubes within  
612 24 h of ICU admission. Plasma was isolated by centrifugation (10 min, 3000 rpm, room  
613 temperature). All samples underwent one freeze-thaw cycle prior to analysis. Proteomic  
614 profiling in urine was completed using the SomaScan® Platform that contains 5,284 SOMAmer  
615 single-stranded DNA aptamers that bind to protein analytes with high specificity. The assays  
616 were performed as previously described (93–95). For each sample, the platform reported a  
617 relative fluorescent unit (RFU) for each aptamer-protein pair that provides a scale-free measure  
618 of protein abundance. The SomaScan Assay is run using 96-well plates, including hybridization  
619 normalization control sequences to control for variability in the Agilent readout process. For  
620 readout, SOMAmer reagents are hybridized to complementary sequences on a DNA microarray  
621 chip and quantified by fluorescence. Fluorescence intensity in the SomaScan assay for each  
622 reagent is related to the relative availability of the three-dimensional shape-charge epitope on  
623 each protein (the binding site of the SOMAmer reagent) in the original sample. This reflects  
624 each protein’s abundance (concentration), the shape of the protein and circulating competitors  
625 (physiologic or a therapeutic antibody). Plate calibration is performed by calculating the ratio of  
626 the Calibrator Reference RFU value to the plate-specific Calibrator replicate median RFU value  
627 for each SOMAmer. The resulting ratio distribution is decomposed into a Plate Scale factor  
628 defined by the median of the distribution and a vector of SOMAmer-specific Calibration Scale  
629 Factors. Median intra- and interassay coefficients of variation are approximately 5% (96).

630

631 **LCB1 Protein expression.** LCB1 design was made as described previously (69). For  
632 expression and purification, briefly, modified pET-29b(+) E. coli plasmid encoding LCB1 was

633 used to transform into chemically competent E. coli Lemo21 cells (NEB). Successfully  
634 transformed E. coli were selected using Studier autoinduction media supplemented with  
635 antibiotics. The cells were harvested by spinning at 4,000xg for 10 min and then resuspended  
636 in a lysis buffer with DNase and protease inhibitors. The cell lysate was sonicated for 4 minutes  
637 total (2 minutes on time, 10 sec on-10 sec off) with an amplitude of 80%. Soluble fraction was  
638 clarified by centrifugation at 20,000g for 30 min and purified by IMAC (Qiagen) followed by size  
639 exclusion chromatography (Superdex 75 10/300 GL, GE Healthcare). All protein samples were  
640 analyzed with SDS-PAGE with the purity higher than 95%. LCB1 spike binders were validated  
641 to neutralize SARS-CoV-2 in Vero cells prior to use in organoids (data not shown).

642

643 **Semi-automated image analysis to quantify SARS-CoV-2-mNG percent infection.**

644 A custom FIJI macro (Sup. file 1) was developed to quantify percent area infected by SARS-  
645 CoV-2-mNG within the entire organoid body as well as within PODXL and LTL positive regions.  
646 This workflow was designed to provide an unbiased approach to quantifying infection, whereas  
647 nuclei-based segmentation of individual cells proved too noisy for accurate quantification due  
648 to the three-dimensional nature of the structures. A representative image analysis workflow is  
649 presented in (S2A-D). For simplicity, quantification was performed on maximum-intensity  
650 projections of confocal Z-stacks taken through the full thickness of the organoid body.  
651 Organoids were manually outlined and the outside signal was cleared to restrict analysis to the  
652 organoid body. For each individual replicate, thresholding parameters were empirically chosen  
653 to accurately define PODXL- and LTL-positive regions and applied uniformly to all mock and  
654 infected organoid images within a paired set. Binary thresholded images were used to define  
655 areas exclusively positive for either PODXL or LTL. Histograms of pixel intensity were generated  
656 for each organoid within its entire outline and sub-regions. Histograms were normalized to  
657 convert raw pixel counts to percent of area, such that each organoid contributes equally to  
658 statistical analysis. To define a threshold for pixel intensity considered infected, normalized pixel

659 intensity histograms of the entire organoid outline for all mock organoids within a particular set  
660 were pooled together and the average and standard deviation (sd) for the pooled data was  
661 quantified. Pixels that were greater than 3 standard deviations above average pixel intensity for  
662 the pooled mock data were defined as infected. Of note, by this criterion for a perfect normal  
663 distribution, mock organoids would be expected to have 0.15% of pixels defined as infected.  
664 The pixel intensity threshold determined from the entire organoid outline was then uniformly  
665 applied to both the PODXL- and LTL- exclusive regions for all organoid images within a set to  
666 determine the percent infection of each region for all organoids.

667

668 **SARS-CoV-2-lentiviral transduction.** Kidney organoids and Vero cells were incubated with  
669 MOI 10 SARS-CoV-2-lentiviral (Amsbio) particles in Opti-MEM reduced serum media (Thermo  
670 Fisher Scientific), incubated for one hour, washed with 1X PBS, and incubated for 48 hours in  
671 RB media prior to 4% paraformaldehyde fixation.

672

673 **Organoid Cell Type Expression Analysis.** An RDS file of publicly available D18-21 hESC-  
674 kidney organoid single cell RNA-seq data (GEO GSE115986) using previously described  
675 clusters was generated using RStudio and Seurat V3 and used to generate a cellxgene (single  
676 cell visualization platform, Chan-Zuckerberg initiative) instance (32). Dot blots representing cell  
677 cluster-specific gene expression were generated using the Visualization in Plugin function.

678

679 **Statistical Analysis.** *Organoid data.* Quantification was performed on data obtained from  
680 experiments performed on controls and treatment conditions side by side on at least three  
681 different occasions or cell lines (biological replicates). Error bars are mean  $\pm$  standard error  
682 (SEM). Statistical analyses were performed using GraphPad Prism Software. Statistical  
683 analyses were only performed for experiments with more than two replicates. Statistics are  
684 plotted on the respective figures and the tests used are described in the figure legends.

685

686 *Clinical Data.* Admission acute kidney injury was defined by comparing the change (delta) and  
687 fold change in concentration from the admission serum creatinine to the lowest serum creatinine  
688 measured in the following 28 days of hospitalization. If the drop in serum creatinine is >0.3  
689 mg/dL or >1.5 fold change the individual was defined as having admission acute kidney injury.

690

691 *Protein Data normalization.* The RFU for each aptamer-protein measurement in each sample  
692 was scaled by dividing it by the mean of the aptamer-protein RFUs reported in that sample to  
693 correct for background variation in RFU. The  $\log_2$  transformation of mean normalized RFU  
694 values was used in regression.

695

696 *Protein Fold change.* We quantified the differences in protein abundance by fold change  
697 calculated as the ratio of normalized RFU values between comparison groups which was then  
698  $\log_2$ -transformed.

699

700 *Protein Regression models.* We performed linear and logistic regression to identify differentially  
701 abundant  $\log_2$  protein outcomes between COVID-positive and COVID-negative patients using  
702 the R `glm()` function. Significant associations were determined after Bonferroni correction ( $0.05$   
703  $/ 4984 = 1 \times 10^{-5}$ ) as well as the false discovery rate (FDR < 0.1 for logistic and <0.05 for linear)  
704 threshold using the Benjamini-Hochberg method. All models were adjusted for age, sex and  
705 BMI. Adjusted  $\log_2$  protein fold changes are the COVID-19+/- beta from the regression model.

706

707 *Pathway Analysis.* The Gene Ontology pathway database is available at the Bader Lab website  
708 ([http://download.baderlab.org/EM\\_Genesets/December\\_11\\_2020/Human/entrezgene/Human](http://download.baderlab.org/EM_Genesets/December_11_2020/Human/entrezgene/Human_GOBP_AllPathways_no_GO_iea_December_11_2020_entrezgene.gmt)  
709 [\\_GOBP\\_AllPathways\\_no\\_GO\\_iea\\_December\\_11\\_2020\\_entrezgene.gmt](http://download.baderlab.org/EM_Genesets/December_11_2020/Human/entrezgene/Human_GOBP_AllPathways_no_GO_iea_December_11_2020_entrezgene.gmt)) (97, 98). Genes IDs  
710 matching 4141 Somalogic protein gene names were identified using the EntrezGene ID in the

711 seq\_gene.md (hg19, GRCh37.3) and the lists of protein-aptamers corresponding to each  
712 pathway were constructed. Pathways with less than three or more than 500 of the identified  
713 protein-aptamer gene names were excluded from analysis, making for 6410 pathways to be  
714 analyzed. The Generalized Berk-Jones test (GBJ) was used with the mean normalized RFU  
715 values of each set of protein-aptamers corresponding to a Gene Ontology pathway. The GBJ  
716 has been shown to be an optimal pathway-based test statistic for aggregated sets of genes,  
717 DNA variants and expression values (99–101). A null model adjusting for sex, age and BMI was  
718 used in each pathway test.

719

720 Statistical analyses relating to the analysis of the clinical and proteomic data were conducted in  
721 R version 3.6.3.

722

723 **Study Approval.** Animal work was performed in compliance with the strict ethical requirements  
724 and regulations of the University of Washington IACUC under a pre-approved animal protocol.  
725 Human samples were collected as part of the CHROME cohort (University of Washington  
726 Institutional Review Board #9763 and #6878). No individual personal data is included in the  
727 study. The IRB provided waiver of consent to participate in this study.

728

729 **Graphical Schematics.** All graphical schematics were originally created with BioRender.com,  
730 aside from Figure 7, which was adapted from “Remdesivir: Potential Repurposed Drug  
731 Candidate for COVID-19”, by BioRender.com (2021). Retrieved from  
732 <https://app.biorender.com/biorender-templates>.

733

734 **Data availability.** All raw data are available upon reasonable request from the corresponding  
735 author. PKD mutant cell lines used in this study may be obtained from the corresponding author  
736 upon request and in accordance with material transfer agreements from the University of

737 Washington and any third-party originating sources. Single-cell data sets are searchable at  
738 <http://nephrocell.miktrmc.org>.

739

#### 740 **CONFLICTS OF INTEREST**

741

742 BSF is an inventor on patent applications related to human kidney organoid differentiation and  
743 modeling of disease in this system. The other authors have declared that no conflict of interest  
744 exists.

745

#### 746 **AUTHOR CONTRIBUTIONS**

747

748 This was a collaborative body of work that was only possible through unique combinations of  
749 expertise from multiple groups. L.H. generated all kidney organoids. S.M., and T-Y. H. prepared  
750 and tittered all viruses. L.H. and S.M. infected organoids. L.H. performed and analyzed LDH  
751 assays. L.H. conducted all immunofluorescence staining in organoids and conducted non-  
752 automated image analysis. B.S.F. conducted immunofluorescence in human kidney tissue  
753 samples. B.J. created the semi-automated image analysis script quantifying the infected kidney  
754 organoid areas. A.K. and S.M. generated *ACE2*<sup>-/-</sup> stem cell lines. S.M. performed  
755 immunohistochemistry on mouse kidney sections. L.H. and B.S.F. performed remdesivir  
756 titrations. L.H., S.S., and Y.T.Z. performed qRT-PCR analyses. S.S. and Y.T.Z. prepared all  
757 LCB1 spike mini spike binder proteins. P.B., C.M., E.M., and M.W., conceived of and designed  
758 the clinical study. R.M. generated .rds file. F.A. analyzed cell gene relationships. I.B.S.  
759 performed all proteomic and clinical data analyses. M.K, J.L.H, C.M., H. R-B., P.B., J. H., M. G.,  
760 and B.S.F supervised the research and secured funding. L.H. and B.S.F. wrote and edited the  
761 first draft of the manuscript. All authors discussed the results and edited the manuscript.

762

763 **ACKNOWLEDGMENTS**

764

765 We thank the Institute for Protein Design and the Baker lab for the LCB1 construct. We thank  
766 and appreciate the helpful discussions with Drs. Julie Mathieu and Shreeram Akilesh. This  
767 research was assisted by Dale Hailey at the University of Washington's Lynn and Mike Garvey  
768 Cell Imaging Core. We thank Tim Martins and the Institute for Stem Cell and Regenerative  
769 Medicine's Quellos High-Throughput Screening Core for screening the spike binders for  
770 efficacy. We would also like to acknowledge the staff at the University of Washington BSL-3  
771 facility and Environmental Health and Safety staff who ensured safety and aided whenever  
772 needed. This work was supported by NIH awards R01DK117914 (BSF), R01DK130386 (BSF),  
773 U01DK127553 (BSF), UH3TR002158 (JH), UG3TR003288 (JH and MK), Department of  
774 Defense award W81XWH2110007 (BSF and HRB), a gift from the Northwest Kidney Centers  
775 to the Kidney Research Institute (BSF), the Lara Nowak Macklin Research Fund (BSF), the  
776 Robert B. McMillen Foundation (CEM, SM), start-up funds from the University of Washington  
777 (BSF), K23DK116967 (PKB), R01DK124063 (PKB), the CDC Foundation (PKB), Roche  
778 Diagnostics (PKB), and the Bill and Melinda Gates Foundation (PKB). Yan Ting Zhao was  
779 supported by NIH T90DE021984. Louisa Helms was supported by NIH 5TL1TR002318-04  
780 (Whitney) and NIH F31DK130550. De-identified human kidney tissue samples were acquired  
781 from the UW Birth Defects Research Laboratory, supported by NIH R24HD000836.

782

783 **REFERENCES**

784

- 785 1. Zhu N et al. A Novel Coronavirus from Patients with Pneumonia in China, 2019. *New*  
786 *England Journal of Medicine* 2020;382(8):727–733.  
787 2. Rabaan AA et al. SARS-CoV-2, SARS-CoV, and MERS-CoV: A comparative  
788 overview. *Infezioni in Medicina* 2020;28(2):174–184.  
789 3. Swai J. Letter to the editor - Mortality rate of acute kidney injury in SARS, MERS, and  
790 COVID-19 infection: A systematic review and meta-analysis. *Critical Care* 2020;24(1):1–  
791 4.

- 792 4. Yeung ML et al. MERS coronavirus induces apoptosis in kidney and lung by  
793 upregulating Smad7 and FGF2. *Nature Microbiology* 2016;1(3):1–8.
- 794 5. Alsaad KO et al. Histopathology of Middle East respiratory syndrome coronavirus  
795 (MERS-CoV) infection – clinicopathological and ultrastructural study. *Histopathology*  
796 2018;72(3):516–524.
- 797 6. Diao B et al. Human kidney is a target for novel severe acute respiratory syndrome  
798 coronavirus 2 infection. *Nature Communications* 2021;12(1):1–9.
- 799 7. Hoffmann M et al. SARS-CoV-2 Cell Entry Depends on ACE2 and TMPRSS2 and Is  
800 Blocked by a Clinically Proven Protease Inhibitor. *Cell* 2020;181(2):271-280.e8.
- 801 8. Wysocki J, Lores E, Ye M, Soler MJ, Battle D. Kidney and Lung ACE2 Expression  
802 after an ACE Inhibitor or an Ang II Receptor Blocker: Implications for COVID-19. *Journal*  
803 *of the American Society of Nephrology* 2020;31(9):1941–1943.
- 804 9. Ye M et al. Glomerular localization and expression of angiotensin-converting enzyme  
805 2 and angiotensin-converting enzyme: Implications for albuminuria in diabetes. *Journal*  
806 *of the American Society of Nephrology* 2006;17(11):3067–3075.
- 807 10. Shang J et al. Cell entry mechanisms of SARS-CoV-2. *Proceedings of the National*  
808 *Academy of Sciences of the United States of America* 2020;117(21).  
809 doi:10.1073/pnas.2003138117
- 810 11. Hamming I et al. Tissue distribution of ACE2 protein, the functional receptor for  
811 SARS coronavirus. A first step in understanding SARS pathogenesis. *Journal of*  
812 *Pathology* 2004;203(2):631–637.
- 813 12. Braun F et al. SARS-CoV-2 renal tropism associates with acute kidney injury. *The*  
814 *Lancet* 2020;396(10251):597–598.
- 815 13. Ramanathan K et al. Histopathology and ultrastructural findings of fatal COVID-19  
816 infections in Washington State: case series 2020;(January):19–21.
- 817 14. Kral AH, Lambdin BH, Wenger LD, Davidson PJ. Evaluation of an Unsanctioned  
818 Safe Consumption Site in the United States. *New England Journal of Medicine*  
819 2020;383(6):589–590.
- 820 15. Hanley B et al. Histopathological findings and viral tropism in UK patients with severe  
821 fatal COVID-19: a post-mortem study. *The Lancet Microbe* 2020;1(6):e245–e253.
- 822 16. Kim JM et al. Original Article Detection and Isolation of SARS-CoV-2 in Serum,  
823 Urine, and Stool Specimens of COVID-19 Patients from the Republic of Korea. *Osong*  
824 *Public Health and Research Perspectives* 2020;11(3):112–117.
- 825 17. Sun J et al. Isolation of infectious SARS-CoV-2 from urine of a COVID-19 patient.  
826 *Emerging Microbes and Infections* 2020;9(1):991–993.
- 827 18. Marchiano S et al. SARS-CoV-2 Infects Human Pluripotent Stem Cell-Derived  
828 Cardiomyocytes, Impairing Electrical and Mechanical Function. *Stem Cell Reports*  
829 2021;16(3):478–492.
- 830 19. Wysocki J et al. A novel soluble ACE2 variant with prolonged duration of action  
831 neutralizes SARS-CoV-2 infection in human kidney organoids. *Journal of the American*  
832 *Society of Nephrology* 2021;32(4):795–803.
- 833 20. Han Y et al. Identification of SARS-CoV-2 inhibitors using lung and colonic  
834 organoids. *Nature* 2021;589(7841):270–275.
- 835 21. Bermejo JAP et al. SARS-CoV-2 infection of human iPSC derived cardiac cells  
836 reflects cytopathic features in hearts of patients with COVID-19. *Science Translational*  
837 *Medicine* 2021;13(590):1–15.
- 838 22. Monteil V et al. Inhibition of SARS-CoV-2 Infections in Engineered Human Tissues  
839 Using Clinical-Grade Soluble Human ACE2. *Cell* 2020;181(4):905-913.e7.
- 840 23. Monteil V et al. Human soluble ACE2 improves the effect of remdesivir in SARS-  
841 CoV-2 infection. *EMBO Molecular Medicine* 2021;13(1):1–8.

842 24. Li M, Izpisua Belmonte JC. Organoids — Preclinical Models of Human Disease. *New*  
843 *England Journal of Medicine* 2019;380(6):569–579.

844 25. Dinnon KH et al. A mouse-adapted model of SARS-CoV-2 to test COVID-19  
845 countermeasures. *Nature* 2020;586(7830):560–566.

846 26. Taguchi A et al. Redefining the in vivo origin of metanephric nephron progenitors  
847 enables generation of complex kidney structures from pluripotent stem cells. *Cell Stem*  
848 *Cell* 2014;14(1):53–67.

849 27. Takasato M et al. Kidney organoids from human iPS cells contain multiple lineages  
850 and model human nephrogenesis. *Nature* 2015;526(7574):564–568.

851 28. Freedman BS et al. Modelling kidney disease with CRISPR-mutant kidney organoids  
852 derived from human pluripotent epiblast spheroids. *Nature Communications*  
853 2015;6(May). doi:10.1038/ncomms9715

854 29. Morizane R et al. Nephron organoids derived from human pluripotent stem cells  
855 model kidney development and injury. *Nature Biotechnology* 2015;33(11):1193–1200.

856 30. Shi P-Y et al. An Infectious cDNA Clone of SARS-CoV-2. *Cell Host and Microbe*  
857 2020;27(May):841–848.

858 31. Wu H et al. Comparative Analysis and Refinement of Human PSC-Derived Kidney  
859 Organoid Differentiation with Single-Cell Transcriptomics. *Cell Stem Cell*  
860 2018;23(6):869-881.e8.

861 32. Harder JL et al. Organoid single cell profiling identifies a transcriptional signature of  
862 glomerular disease. *JCI Insight* 2019;4(1). doi:10.1172/jci.insight.122697

863 33. Czerniecki SM et al. High-Throughput Screening Enhances Kidney Organoid  
864 Differentiation from Human Pluripotent Stem Cells and Enables Automated  
865 Multidimensional Phenotyping. *Cell Stem Cell* 2018;22(6):929-940.e4.

866 34. Omer D et al. Human Kidney Spheroids and Monolayers Provide Insights into SARS-  
867 CoV-2 Renal Interactions. *Journal of the American Society of Nephrology*  
868 2021;ASN.2020111546.

869 35. Kim YK et al. Gene-Edited Human Kidney Organoids Reveal Mechanisms of  
870 Disease in Podocyte Development. *Stem Cells* 2017;35(12):2366–2378.

871 36. Tanigawa S et al. Organoids from Nephrotic Disease-Derived iPSCs Identify  
872 Impaired NEPHRIN Localization and Slit Diaphragm Formation in Kidney Podocytes.  
873 *Stem Cell Reports* 2018;11(3):727–740.

874 37. Cruz NM et al. Organoid cystogenesis reveals a critical role of microenvironment in  
875 human polycystic kidney disease. *Nature Materials* 2017;16(11):1112–1119.

876 38. Giroglou T et al. Retroviral Vectors Pseudotyped with Severe Acute Respiratory  
877 Syndrome Coronavirus S Protein. *Journal of Virology* 2004;78(17):9007–9015.

878 39. Henry BM, Lippi G. Chronic kidney disease is associated with severe coronavirus  
879 disease 2019 (COVID-19) infection. *International Urology and Nephrology*  
880 2020;52(6):1193–1194.

881 40. Bhatraju PK et al. Comparison of host endothelial, epithelial and inflammatory  
882 response in ICU patients with and without COVID-19: a prospective observational cohort  
883 study. *Critical Care* 2021;25(1):1–12.

884 41. Menon R et al. SARS-CoV-2 receptor networks in diabetic and COVID-19–  
885 associated kidney disease. *Kidney International* 2020;98(6):1502–1518.

886 42. Zhu L et al. Single-Cell Sequencing of Peripheral Mononuclear Cells Reveals  
887 Distinct Immune Response Landscapes of COVID-19 and Influenza Patients. *Immunity*  
888 2020;53(3):685-696.e3.

889 43. Lee JS, Shin EC. The type I interferon response in COVID-19: implications for  
890 treatment. *Nature Reviews Immunology* 2020;20(10):585–586.

891 44. Zhou Z et al. Heightened Innate Immune Responses in the Respiratory Tract of  
892 COVID-19 Patients. *Cell Host and Microbe* 2020;27(6):883-890.e2.

893 45. Sinuani I, Beberashvili I, Averbukh Z, Sandbank J. Role of IL-10 in the progression of  
894 kidney disease. *World Journal of Transplantation* 2013;3(4):91.  
895 46. Duffy S. Why are RNA virus mutation rates so damn high?. *PLoS Biology*  
896 2018;16(8):1–6.  
897 47. Plante JA et al. Spike mutation D614G alters SARS-CoV-2 fitness. *Nature*  
898 2021;592(7852):116–121.  
899 48. Luring AS, Hodcroft EB. Genetic Variants of SARS-CoV-2 - What Do They Mean?.  
900 *JAMA - Journal of the American Medical Association* 2021;325(6):529–531.  
901 49. Abdelnabi R et al. Comparing infectivity and virulence of emerging SARS-CoV-2  
902 variants in Syrian hamsters. *EBioMedicine* 2021;68:103403.  
903 50. Panzera Y et al. A deletion in SARS-CoV-2 ORF7 identified in COVID-19 outbreak in  
904 Uruguay. *Transboundary and Emerging Diseases* 2021;(December 2020):1–8.  
905 51. Foster CSP, Rawlinson WD. Rapid spread of a SARS-CoV-2 Delta variant with a  
906 frameshift deletion in ORF7a. *medRxiv* 2021;(August):2021.08.18.21262089.  
907 52. Feder KA, Pearlowitz M, Goode A, Duwell M, Williams TW. Linked Clusters of  
908 SARS-CoV-2 Variant B.1.1.351 — Maryland, January – February  
909 2021. *MMWR* 2021;70(17):627–631.  
910 53. Firestone MJ et al. First Identified Cases of SARS-CoV-2 Variant P.1 in the United  
911 States — Minnesota, January 2021. *MMWR Surveillance Summaries* 2021;70(10):345–  
912 346.  
913 54. States U, Galloway SE, Paul P, Maccannell DR, Johansson MA. Emergence of  
914 SARS-CoV-2 B.1.1.7 Lineage — 2021;70(3):95–99.  
915 55. Bedford T et al. Cryptic transmission of SARS-CoV-2 in Washington state. *Science*  
916 2020;370(6516):571–575.  
917 56. Nam SA et al. Graft immaturity and safety concerns in transplanted human kidney  
918 organoids. *Experimental and Molecular Medicine* 2019;51(11). doi:10.1038/s12276-019-  
919 0336-x  
920 57. Verdecchia P, Cavallini C, Spanevello A, Angeli F. The pivotal link between ACE2  
921 deficiency and SARS-CoV-2 infection. *Elsevier* 2020;(January):14–20.  
922 58. Twomey JD et al. COVID-19 update: The race to therapeutic development. *Drug*  
923 *Resistance Updates* 2020;53(October):100733.  
924 59. Wang Y et al. Remdesivir in adults with severe COVID-19: a randomised, double-  
925 blind, placebo-controlled, multicentre trial. *The Lancet* 2020;395(10236):1569–1578.  
926 60. Thakare S et al. Safety of Remdesivir in Patients With Acute Kidney Injury or CKD.  
927 *Kidney International Reports* 2021;6(1):206–210.  
928 61. Chouchana, Laurent, Preta, Laure-Helene, Tisseyre, Mylene, Terrier, Benjamin,  
929 Treluyer, Jean-Marc, Montastruc F. Kidney disorders as serious adverse drug reactions  
930 of remdesivir in coronavirus disease 2019: a retrospective case-noncase  
931 study. 2020;(January).  
932 62. Adamsick ML et al. Remdesivir in patients with acute or chronic kidney disease and  
933 COVID-19. *Journal of the American Society of Nephrology* 2020;31(7):1384–1386.  
934 63. Repurposed Antiviral Drugs for Covid-19 — Interim WHO Solidarity Trial Results.  
935 *New England Journal of Medicine* 2021;384(6):497–511.  
936 64. Barratt-Due A et al. Evaluation of the Effects of Remdesivir and Hydroxychloroquine  
937 on Viral Clearance in COVID-19. *Annals of Internal Medicine* [published online ahead of  
938 print: 2021]; doi:10.7326/m21-0653  
939 65. Cao L et al. De novo design of picomolar SARS-CoV-2 miniprotein inhibitors.  
940 *Science* 2020;370(6515):426–431.  
941 66. Case JB et al. Ultrapotent miniproteins targeting the SARS-CoV-2 receptor-binding  
942 domain protect against infection and disease. *Cell Host and Microbe* 2021;29(7):1151-  
943 1161.e5.

944 67. Howden SE et al. Plasticity of distal nephron epithelia from human kidney organoids  
945 enables the induction of ureteric tip and stalk. *Cell Stem Cell* 2021;28(4):671-684.e6.  
946 68. Cui X, Gallini JW, Jasien CL, Mrug M. Autosomal Dominant Polycystic Kidney  
947 Disease does not significantly alter major COVID-19 outcomes among veterans.  
948 *Kidney360* 2021;2:10.34067/KID.0007282020.  
949 69. Xu J et al. SARS-CoV-2 induces transcriptional signatures in human lung epithelial  
950 cells that promote lung fibrosis. *Respiratory Research* 2020;21(1):1-12.  
951 70. Zhang M et al. Biomimetic Human Disease Model of SARS-CoV-2-Induced Lung  
952 Injury and Immune Responses on Organ Chip System. *Advanced Science* 2021;8(3):1-  
953 14.  
954 71. Chilosi M et al. The pathogenic role of epithelial and endothelial cells in early-phase  
955 COVID-19 pneumonia: victims and partners in crime. *Modern Pathology* [published  
956 online ahead of print: 2021]; doi:10.1038/s41379-021-00808-8  
957 72. Lazzeri E et al. Endocycle-related tubular cell hypertrophy and progenitor  
958 proliferation recover renal function after acute kidney injury. *Nature Communications*  
959 2018;9(1):1-18.  
960 73. Järhult JD, Hultström M, Bergqvist A, Frithiof R, Lipcsey M. The impact of viremia on  
961 organ failure, biomarkers and mortality in a Swedish cohort of critically ill COVID-19  
962 patients. *Scientific Reports* 2021;11(1):1-8.  
963 74. Li Y et al. SARS-CoV-2 viremia is associated with distinct proteomic pathways and  
964 predicts COVID-19 outcomes. *Journal of Clinical Investigation* 2021;131(13).  
965 doi:10.1172/JCI148635  
966 75. Myhre PL, Prebensen C, Jonassen CM, Berdal JE, Omland T. Sars-cov-2 viremia is  
967 associated with inflammatory, but not cardiovascular biomarkers, in patients hospitalized  
968 for covid-19. *Journal of the American Heart Association* 2021;10(9):1-5.  
969 76. Shetty AA et al. COVID-19-associated glomerular disease. *Journal of the American*  
970 *Society of Nephrology* 2021;32(1):33-40.  
971 77. Kissling S et al. Collapsing glomerulopathy in a COVID-19 patient. *Kidney*  
972 *International* 2020;98(1):228-231.  
973 78. Reich HN, Oudit GY, Penninger JM, Scholey JW, Herzenberg AM. Decreased  
974 glomerular and tubular expression of ACE2 in patients with type 2 diabetes and kidney  
975 disease. *Kidney International* 2008;74(12):1610-1616.  
976 79. Liu E et al. Profiling APOL1 Nephropathy Risk Variants in Genome-Edited Kidney  
977 Organoids with Single-Cell Transcriptomics. *Kidney360* 2020;1(3):203-215.  
978 80. Beckerman P et al. Transgenic expression of human APOL1 risk variants in  
979 podocytes induces kidney disease in mice. *Nature Medicine* 2017;23(4):429-438.  
980 81. Aghajan M et al. Antisense oligonucleotide treatment ameliorates IFN- $\gamma$ -induced  
981 proteinuria in APOL1-transgenic mice. *JCI Insight* 2019;4(12):0-19.  
982 82. Nichols B et al. Innate immunity pathways regulate the nephropathy gene  
983 Apolipoprotein L1. *Kidney International* 2015;87(2):332-342.  
984 83. EMA. Summary on compassionate use Remdesivir Gilead International  
985 Nonproprietary Name : remdesivir . *European Medicines Agency* 2020;31(April):41.  
986 84. Tempestilli M et al. Pharmacokinetics of remdesivir and GS-441524 in two critically ill  
987 patients who recovered from COVID-19. *Journal of Antimicrobial Chemotherapy*  
988 2020;75(10):2977-2980.  
989 85. Hunt AC et al. Multivalent designed proteins protect against SARS-CoV-2 variants of  
990 concern. *bioRxiv* 2021;2021.07.07.451375.  
991 86. Rodrigues C. Clinical Infectious Diseases Society Clinical Infectious Diseases  
992 Society2021;(Xx Xxxx):2-3.

993 87. Khan A et al. Higher infectivity of the SARS-CoV-2 new variants is associated with  
994 K417N/T, E484K, and N501Y mutants: An insight from structural data. *Journal of*  
995 *Cellular Physiology* 2021;(March):1–13.

996 88. Cheng MH, Krieger JM, Kaynak B, Arditi M, Bahar I. Impact of South African 501.V2  
997 variant on SARS-CoV-2 spike infectivity and neutralization: A structure-based  
998 computational assessment. *bioRxiv* [published online ahead of print: 2021];  
999 doi:10.1101/2021.01.10.426143

1000 89. Redondo N, Zaldívar-López S, Garrido JJ, Montoya M. SARS-CoV-2 Accessory  
1001 Proteins in Viral Pathogenesis: Knowns and Unknowns. *Frontiers in Immunology*  
1002 2021;12(December 2019):1–8.

1003 90. Sims AC et al. Severe Acute Respiratory Syndrome Coronavirus Infection of Human  
1004 Ciliated Airway Epithelia: Role of Ciliated Cells in Viral Spread in the Conducting Airways  
1005 of the Lungs. *Journal of Virology* 2005;79(24):15511–15524.

1006 91. Charytan DM et al. Decreasing Incidence of Acute Kidney Injury in Patients with  
1007 COVID-19 Critical Illness in New York City. *Kidney International Reports* 2021;6(4):916–  
1008 927.

1009 92. Smith KD, Akilesh S. Pathogenesis of coronavirus disease 2019-associated kidney  
1010 injury. *Current opinion in nephrology and hypertension* 2021;30(3):324–331.

1011 93. Rohloff JC et al. Nucleic acid ligands with protein-like side chains: Modified aptamers  
1012 and their use as diagnostic and therapeutic agents. *Molecular Therapy - Nucleic Acids*  
1013 2014;3(October):e201.

1014 94. Williams SA et al. Plasma protein patterns as comprehensive indicators of health.  
1015 *Nature Medicine* 2019;25(12):1851–1857.

1016 95. Kim CH et al. Stability and reproducibility of proteomic profiles measured with an  
1017 aptamer-based platform. *Scientific Reports* 2018;8(1):1–10.

1018 96. Candia J et al. Assessment of Variability in the SOMAscan Assay. *Scientific Reports*  
1019 2017;7(1):1–13.

1020 97. Merico D, Isserlin R, Stueker O, Emili A, Bader GD. Enrichment map: A network-  
1021 based method for gene-set enrichment visualization and interpretation. *PLoS ONE*  
1022 2010;5(11). doi:10.1371/journal.pone.0013984

1023 98. Gene T, Consortium O. Gene Ontology : tool for the . *Gene Expression*  
1024 2000;25(may):25–29.

1025 99. Sun R, Hui S, Bader GD, Lin X, Kraft P. Powerful Gene Set Analysis in GWAS with  
1026 the Generalized Berk-Jones Statistic. *Powerful gene set analysis in GWAS with the*  
1027 *generalized berk-jones statistic* 2018;361436.

1028 100. Gaynor SM, Sun R, Lin X, Quackenbush J. Identification of differentially expressed  
1029 gene sets using the Generalized Berk-Jones statistic. *Bioinformatics* 2019;35(22):4568–  
1030 4576.

1031 101. Sun R, Lin X. Genetic Variant Set-Based Tests Using the Generalized Berk–Jones  
1032 Statistic With Application to a Genome-Wide Association Study of Breast Cancer.  
1033 *Journal of the American Statistical Association* 2020;115(531):1079–1091.

1034

1035

1036

1037

**Figure 1: SARS-CoV2 efficiently infects human kidney organoids with tropism for proximal tubules**

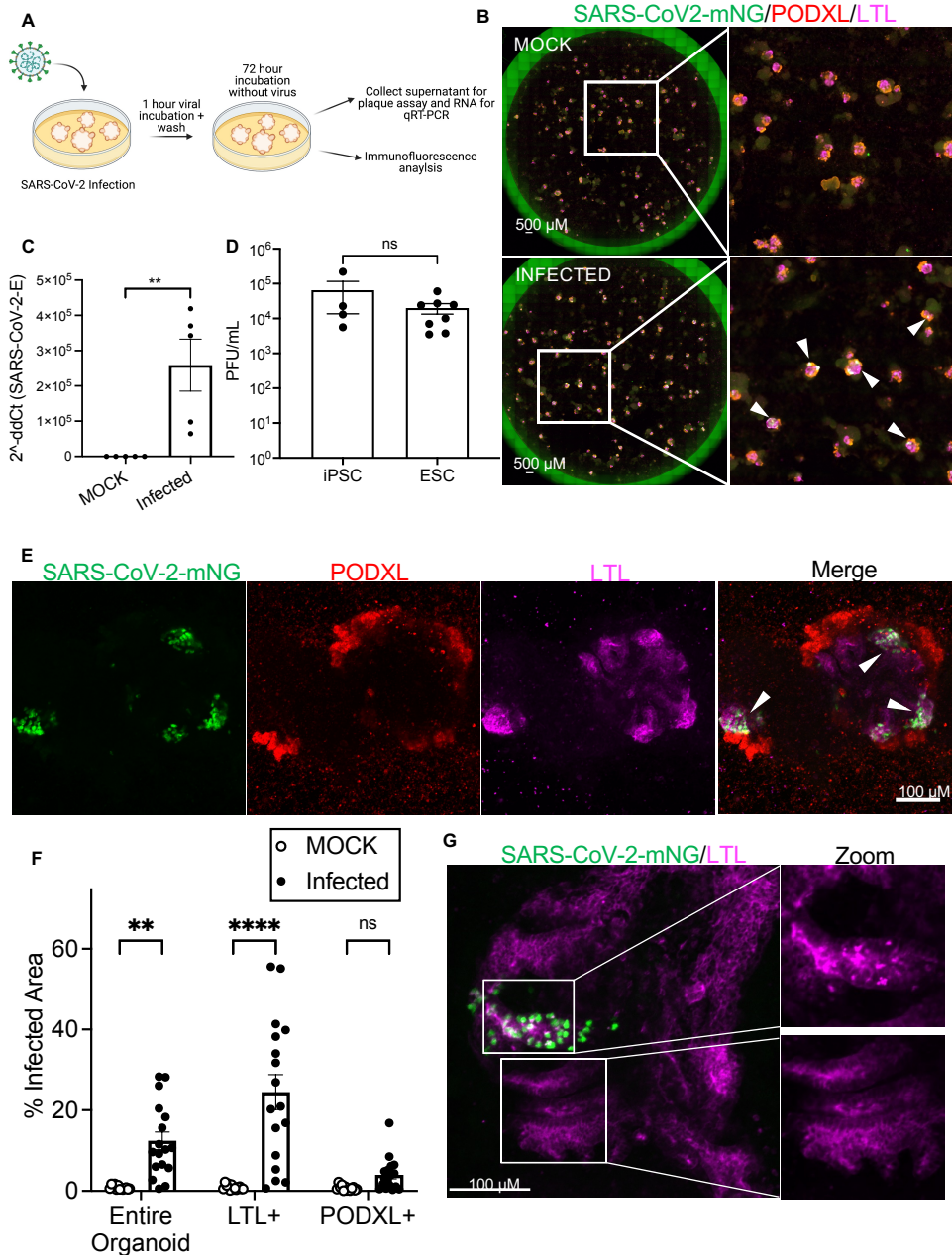


**Figure 1. SARS-CoV2 efficiently infects human kidney organoids with tropism for proximal tubules** A. Schematic of kidney organoid infection protocol. B. Whole well wide-field immunofluorescence images of iPS cell-derived organoids infected with SARS-CoV2-mNG. Arrows point to infected cells. C. qRT-PCR of SARS-CoV-2 envelope RNA in organoids infected with SARS-CoV-2 WA1 or mock-infected (MOCK). Dots represent a well of organoids. Mean  $\pm$  SEM,  $n \geq 1$  well of organoids per infection from four independent experiments. Mann-Whitney test, \*\* $p < 0.01$ . D. Plaque assays of SARS-CoV-2 infected human kidney organoids derived from iPS cells or ES cells. Dots represent a well of organoids. Mean  $\pm$  SEM,  $n \geq 1$  well of organoids per infection from three independent experiments respectively. Mann-Whitney test, ns  $p > 0.05$ . E. Representative confocal immunofluorescence images of organoids infected with SARS-CoV2-mNG. F. Quantification of infected organoid cellular tropism. Dots represent a single organoid. Mean  $\pm$  SEM,  $n \geq 4$  organoids per infection from three independent experiments. 2-way ANOVA, multiple comparisons MOCK vs infected for each respective region. \*\* $p < 0.01$ , \*\*\*\* $p < 0.0001$ , ns  $p > 0.05$ . G. Representative confocal immunofluorescence images of organoid infected with SARS-CoV2-GFP, with zoomed images of white boxed areas showing infected (top) versus uninfected (bottom) proximal tubules. Arrowheads indicate areas of disrupted LTL pattern.

**Figure 2: SARS-CoV-2 infects PKD organoid cystic epithelium**

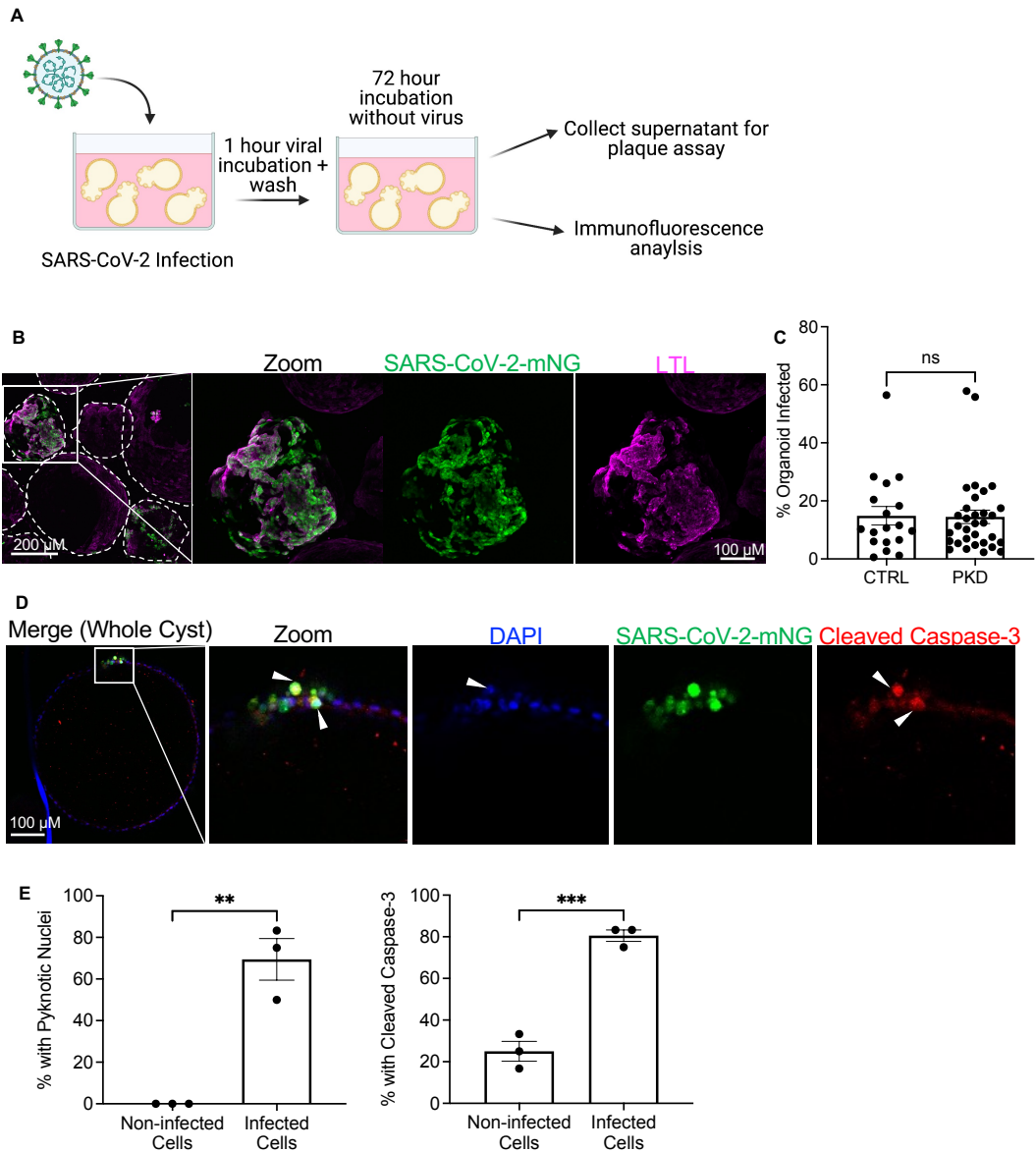


**Figure 2. SARS-CoV-2 infects PKD organoid cystic epithelium.** A. Schematic of cystic PKD organoid infection protocol. B. Representative confocal immunofluorescence images showing cystic PKD organoids infected with SARS-CoV2-mNG. Outlines denote independent organoids. C. Quantification of infected organoid area (% total) of PKD and control (isogenic non-PKD) SARS-CoV-2-mNG infected cultures. Dots represent a single organoid. Mean  $\pm$  SEM,  $n \geq 4$  organoids per infection from three independent experiments each. Unpaired t-test, ns  $p > 0.05$ . D. Representative immunofluorescence images of cystic PKD organoids infected with SARS-CoV2-mNG, with zoom of cleaved caspase-3 staining and pyknotic nuclei. E. Quantification of pyknotic nuclei and elevated cleaved caspase-3 levels of infected and non-infected cells of infected organoids. Dots represent a biological replicate. Mean  $\pm$  SEM,  $n \geq 5$  organoids per biological replicate from three independent experiments each. Unpaired t-test, \*\* $p < 0.01$ , \*\*\* $p < 0.001$ .

**Figure 3: COVID-19<sup>+</sup> patient urine expresses signatures found in organoids**

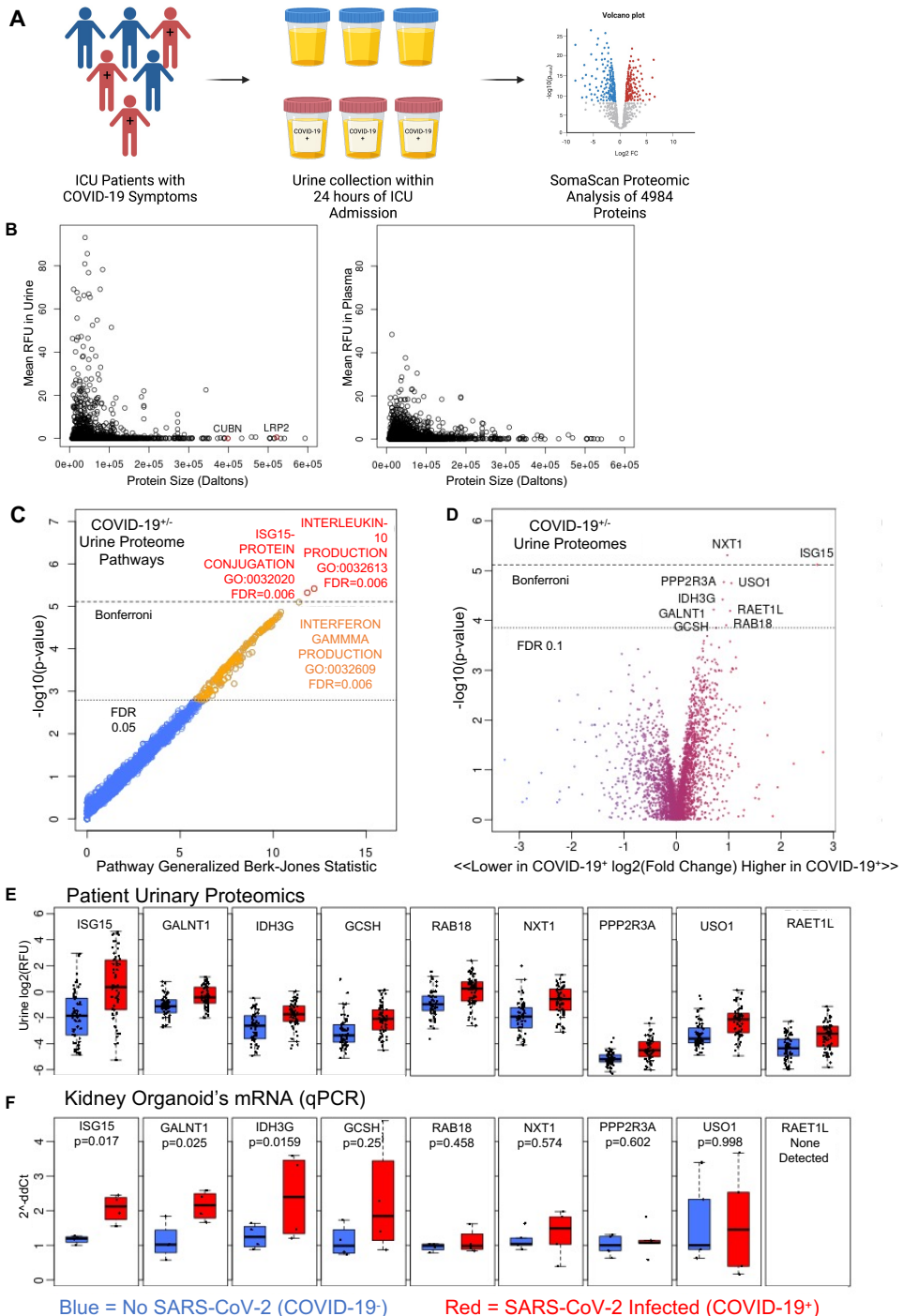


**Figure 3. COVID-19<sup>+</sup> patient urine expresses signatures found in organoids.** A. Schematic of patient cohort sample selection and analysis. B. Scatterplots of protein size vs relative abundance units (RFU) detected in patient urine and patient blood. C. Gene ontology pathway analysis of urine proteome reads. Red circles represent pathways that hit Bonferroni significance, orange circles represent pathways that hit an FDR <0.05, and blue are non-significant pathways. D. Volcano plot of increased and decreased proteins in COVID-19<sup>+</sup> patient urine compared to COVID-19<sup>-</sup> patient urine. Dotted lines represent FDR 0.1 and Bonferroni significance cutoffs. E. Upregulated proteomic hits between COVID-19<sup>+</sup> and COVID-19<sup>-</sup> patients. F. qRT-PCR of upregulated proteomic hits in organoids infected with SARS-CoV-2 WA1 or mock-infected (MOCK). Dots represent a well of organoids. Mean ± SEM, n ≥ 1 well of organoids per infection from four independent experiments. Unpaired t-test, \*p < 0.05.

**Figure 4: SARS-CoV-2 variants show similar rates of infection in kidney organoids**

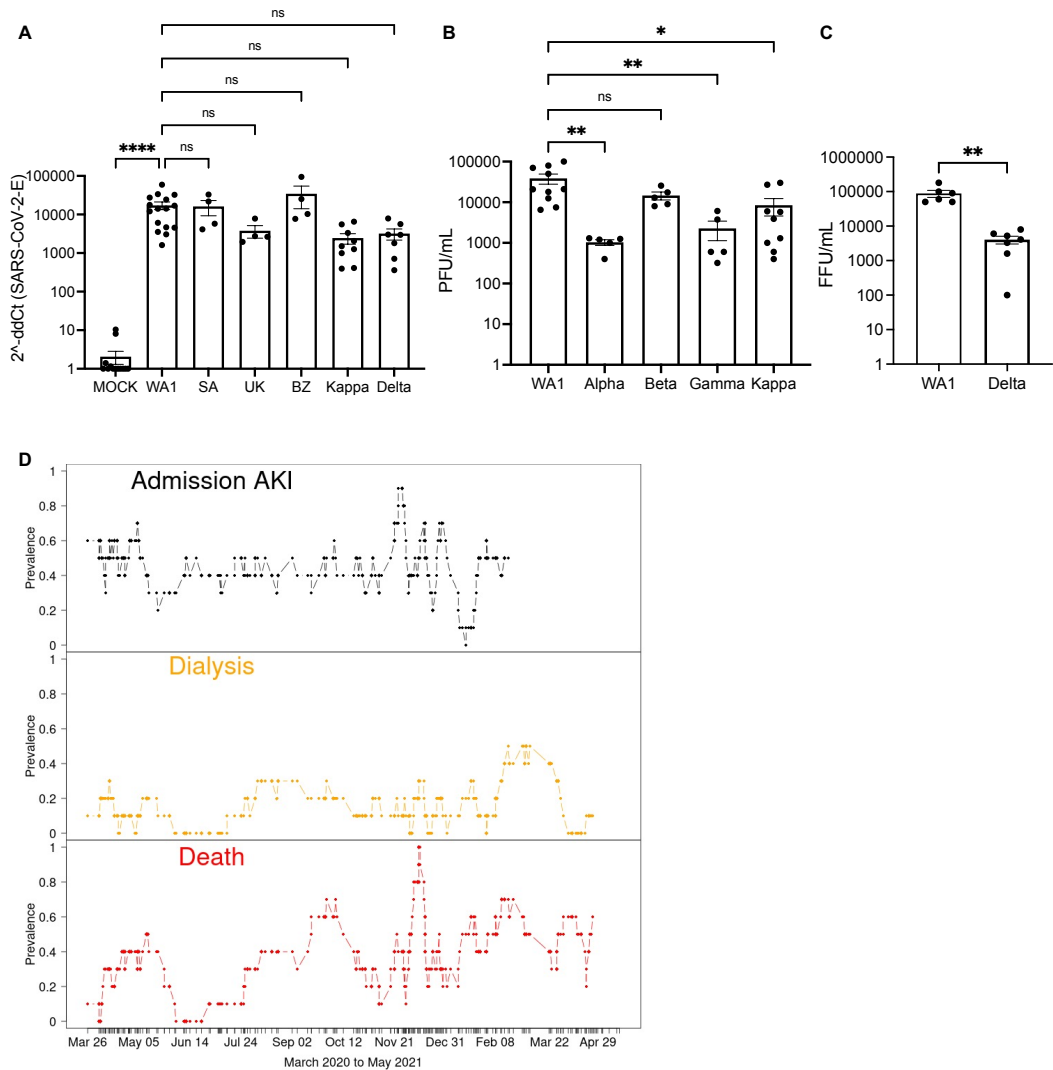


**Figure 4. SARS-CoV-2 variants show similar rates of infection in kidney organoids.** A. qRT-PCR of SARS-CoV-2 envelope RNA in infected kidney organoid cultures. Dots represent a well of organoids. Mean  $\pm$  SEM,  $n \geq 1$  well of organoids per infection from three independent experiments. One-way ANOVA, Kruskal-Wallis post-hoc test,  $**p < 0.01$ ,  $ns p > 0.05$ . B. Plaque assays of SARS-CoV-2 infected kidney organoids. Dots represent a well of organoids. Mean  $\pm$  SEM,  $n \geq 1$  well of organoids per infection from three independent experiments. One-way ANOVA, Kruskal-Wallis post-hoc test,  $*p < 0.05$ ,  $ns p > 0.05$ . C. Focus forming assay of SARS-CoV-2 infected kidney organoids. Dots represent a well of organoids. Mean  $\pm$  SEM,  $n \geq 1$  biological replicates per condition from three independent experiments. Mann-Whitney test,  $**p < 0.01$ . D. Prevalence of admission AKI, dialysis, and death in COVID+ patients over time.

**Figure 5: ACE2 is an essential viral entry pathway for SARS-CoV-2 infection of kidney organoids**

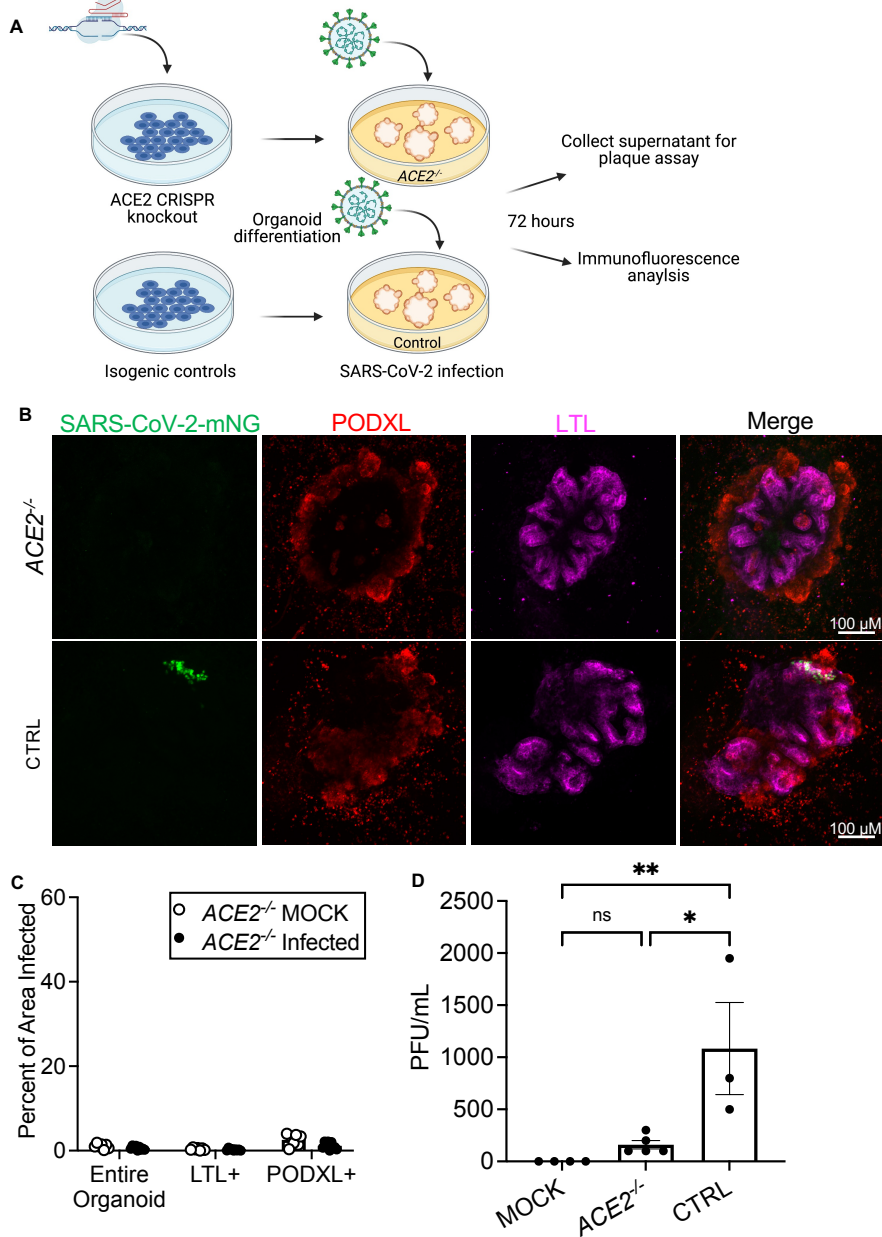


**Figure 5. ACE2 is an essential viral entry pathway for SARS-CoV-2 infection of kidney organoids.** A. Schematic of ACE2 knockout and infection protocol. B. Representative confocal immunofluorescence images of ACE2<sup>-/-</sup> SARS-CoV2-mNG infected organoids, compared to isogenic controls. C. Quantification of GFP+ area in ACE2<sup>-/-</sup> organoids infected with SARS-CoV2-mNG, compared to mock-treated control. Dots represent a single organoid. N ≥ 4 organoids per experiment from two experiments. D. Plaque assay of ACE2<sup>-/-</sup> and control organoids infected with SARS-CoV-2 or mock-treated. Non-log scale is shown for this figure to emphasize low levels of infection in ACE2<sup>-/-</sup> organoids. Dots represent a well of organoids. Mean ± SEM, n ≥ 1 well of organoids per infection from three independent experiments, utilizing two distinct mutant cell lines. One-way ANOVA with Tukey's post-hoc tests. \*p < 0.05, \*\*p < 0.01, ns p > 0.05.

**Figure 6: Therapeutic interventions reduce SARS-CoV-2 infection and replication in human kidney organoids**

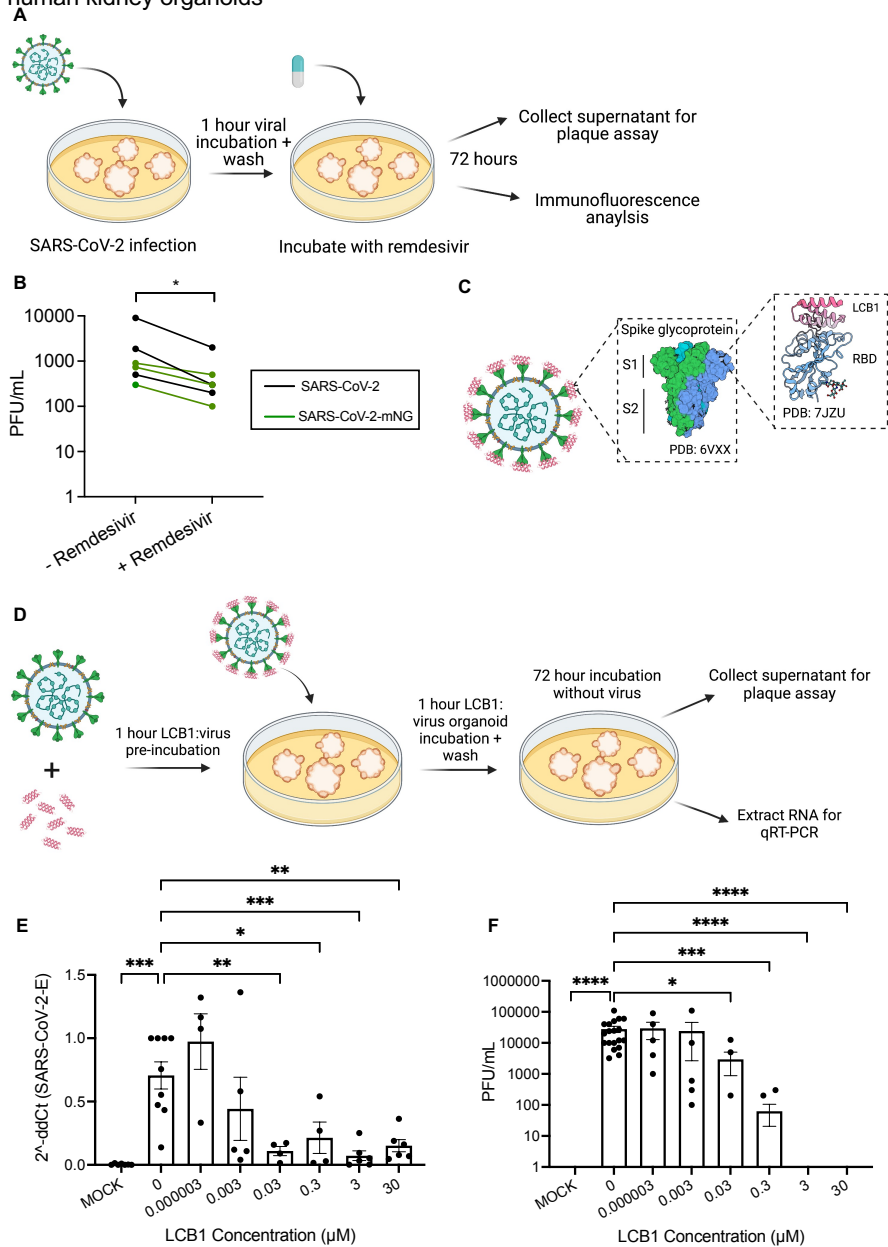


**Figure 6. Therapeutic interventions reduce SARS-CoV-2 infection and replication in human kidney organoids.** A. Schematic of protocol for SARS-CoV-2 kidney organoid infection with remdesivir treatment. B. Plaque assays of SARS-CoV2 and SARS-CoV-2-mNG infected kidney organoids treated with or without remdesivir. Mean  $\pm$  SEM of three independent experiments. Wilcoxon matched-pairs signed rank test, \* $p < 0.05$ . C. Schematic of LCB1 binding to spike glycoprotein receptor binding domain (RBD). D. Schematic of LCB1 viral pre-treatment and infection of kidney organoids. E. qRT-PCR expression levels of SARS-CoV-2 envelope RNA in infected kidney organoid cultures, with increasing levels of LCB1 protein pre-incubated with virus. Dots represent a well of organoids. Mean  $\pm$  SEM,  $n \geq 1$  well of organoids per infection from four independent experiments, 2 iPS and 2 ES, normalized to beta-actin. One-way ANOVA, Kruskal-Wallis post-hoc test, \* $p < 0.05$ , \*\* $p < 0.01$ , \*\*\*\* $p < 0.0001$ , ns  $p > 0.05$ . F. Plaque assays of SARS-CoV2 infected kidney organoids with increasing levels of LCB1 protein pre-incubated with virus. Dots represent a well of organoids. Mean  $\pm$  SEM,  $n \geq 1$  well of organoids per infection from four independent experiments: 2 iPS and 2 ES. One-way ANOVA, Kruskal-Wallis post-hoc test, \* $p < 0.05$ , \*\* $p < 0.01$ , \*\*\*\* $p < 0.0001$ , ns  $p > 0.05$ .

1115 **TABLES**1116 **Table 1:** Demographics and clinical outcomes of patient cohort

	<b>COVID-19 Negative (N=59)</b>	<b>COVID-19 Positive (N=61)</b>
<b>Age, Mean (SD)</b>	53.7 (16.3)	55.7 (17.1)
<b>Male</b>	32 (54.2%)	46 (75.4%)
<b>Race</b>		
White	34 (57.6%)	39 (63.9%)
Asian	5 (8.5%)	7 (11.5%)
Black	12 (20.3%)	5 (8.2%)
Native American	3 (5.1%)	4 (6.6%)
Unknown	5 (8.5%)	6 (9.8%)
<b>Ethnicity</b>		
Hispanic or Latino	4 (6.8%)	23 (37.7%)
NOT Hispanic or Latino	51 (86.4%)	35 (57.4%)
Unknown	4 (6.8%)	3 (4.9%)
<b>Asthma</b>	12 (20.3%)	6 (9.8%)
<b>Diabetes</b>	18 (30.5%)	20 (32.8%)
<b>Chronic Kidney Disease</b>	10 (16.9%)	6 (9.8%)
<b>Coronary Artery Disease</b>	13 (22.0%)	7 (11.7%)
<b>Congestive Heart Failure</b>	19 (32.2%)	10 (16.4%)
<b>NIH Ordinal Scale on Admission</b>		
Hospitalized	12 (20.3%)	11 (18.0%)
Hospitalized, requiring non-invasive positive pressure ventilation, high flow nasal cannula or non-rebreather	6 (10.2%)	4 (6.6%)
Hospitalized, requiring invasive mechanical ventilation or extracorporeal membrane oxygenation	41 (69.5%)	46 (75.4%)
<b>AKI at the time of Study Enrollment</b>	35 (59.3%)	35 (58.3%)
<b>Inpatient Dialysis</b>	4 (6.8%)	9 (14.8%)
<b>In-hospital Mortality</b>	20 (33.9%)	22 (36.1%)

1117 **Table 2:** Viral variant descriptions

Origin	Lineage	GISAID Clade	WHO Label
USA-WA1	A	S	NA
United Kingdom	B.1.1.7	GR	Alpha
South African	B.1.351-HV001	GH	Beta
Brazil	P.1	GR	Gamma
India	B.1.617.1	G	Kappa
India	B.1.617.2	G	Delta

1118

1119

1120

1121

1122

1123

1124

1125

1126

1127

1128

1129

1130

1131

1132

1133